Transition energies and direct-indirect band gap crossing in zinc-blende Al$_x$Ga$_{1-x}$N

M. Landmann,[*] E. Rauls, and W. G. Schmidt

Lehrstuhl für Theoretische Physik, Universität Paderborn, 33095 Paderborn, Germany

Marcus Röppischer, Christoph Cobet, and Norbert Esser

Leibniz-Institut für Analytische Wissenschaften - ISAS - e.V., Albert-Einstein-Str. 9, 12489 Berlin, Germany

Thorsten Schupp and Donat J. As

Experimentalphysik, University of Paderborn, Warburger Str. 100, 33098 Paderborn, Germany

Martin Feneberg and Rüdiger Goldhahn

Institut für Experimentelle Physik, Otto-von-Guericke-Universität Magdeburg, Universitätsplatz 2, 39106 Magdeburg, Germany

The electronic and optical properties of zinc-blende (zb) Al$_x$Ga$_{1-x}$N over the whole alloy composition range are presented in a joint theoretical and experimental study. Because zb-GaN is a direct ($\Gamma_v \rightarrow \Gamma_c$) semiconductor and zb-AlN shows an indirect ($\Gamma_v \rightarrow X_c$) fundamental band gap, the ternary alloy exhibits a concentration-dependent direct-indirect band gap crossing point the position of which is highly controversial. The dielectric functions of zb-Al$_x$Ga$_{1-x}$N alloys are measured employing synchrotron-based ellipsometry in an energy range between 1 and 20 eV. The experimentally determined fundamental energy transitions originating from the Γ, X, and L points are identified by comparison to theoretical band-to-band transition energies. In order to determine the direct-indirect band gap crossing point, the measured transition energies at the X point have to be aligned by the calculated position of the highest valence state. Thereby density-functional theory (DFT) based approaches to the electronic structure, ranging from the standard (semi)local generalized gradient approximation (GGA), self-energy corrected local density approximation (LDA-1/2), and meta-GGA DFT (TB-mBJLDA) to hybrid functional DFT and many-body perturbation theory in the GW approximation, are applied to random and special quasirandom structure models of zb-Al$_x$Ga$_{1-x}$N. This study provides interesting insights into the accuracy of the various numerical approaches and contains reliable *ab initio* data on the electronic structure and fundamental alloy band gaps of zb-Al$_x$Ga$_{1-x}$N. Nonlocal Heyd-Scuseria-Ernzerhof-type hybrid-functional DFT calculations or, alternatively, GW quasiparticle calculations are required to reproduce prominent features of the electronic structure. The direct-indirect band gap crossing point of zb-Al$_x$Ga$_{1-x}$N is found in the Al rich composition range at an Al content between $x = 0.64$ and 0.69 in hybrid functional DFT, which is in good agreement with $x = 0.71$ determined from the aligned experimental transition energies. Thus our study solves the long-standing debate on the nature of the fundamental zb-Al$_x$Ga$_{1-x}$N alloy band gap.

I. INTRODUCTION

Throughout the last two decades, scientific breakthroughs on the field of group-III nitride semiconductor materials have always stimulated rapid technological progress in the manufacturing of optoelectronic and electronic devices. Group-III nitrides naturally crystallize in stable hexagonal lattices with wurtzite (wz) structure (space group: $P6_3mc - C_{6v}^4$). Artificially grown, group-III nitrides may adopt a metastable cubic phase with a zinc-blende (zb) structure (space group: $F\bar{4}3m - T_d^2$). Probably the most appealing characteristic of binary group-III nitrides and their multicomponent alloys is the extremely large accessible range of band gap energies, i.e., from ∼0.7 eV (wz-InN)[1] to ∼6.0 eV (wz-AlN)[2,3] for the hexagonal compounds and from ∼0.6 eV (zb-InN)[4] to ∼5.3 eV (zb-AlN)[5] for the cubic ones.

For a long time almost exclusively grown along the polar (0001) c direction of the hexagonal crystal, group-III nitrides, and their multicomponent alloys exhibit strong internal piezoelectric and spontaneous polarization electric fields, which are undesirable for optoelectronic applications since they inherently limit the device performance.[6,7] The occurrence of such polarization fields is a direct consequence of the lack of inversion symmetry in the hexagonal crystal that naturally show both piezoelectric and spontaneous polarization parallel to the c axis.[8] The growth of nonpolar and semipolar nitrides has found increasing technological interest over the past years to avoid these strong internal fields. In these nonpolar or semipolar nitrides, the c axis is orthogonal or inclined to the growth direction, thus eliminating or limiting the field effects in the growth direction.[9] However, the electrical, optical, and structural properties are affected by strong lateral anisotropies. A way to fabricate group-III nitride based optoelectronic devices, fundamentally free of polarization fields,[7] is the growth[5,10–14] of cubic nitride alloys with (001) orientation and the engineering of nanostructured material compounds (e.g., quantum wells and superlattices).[15–20]

Among all group-III nitride semiconductors, zb-AlN is the only binary semiconductor with an nondirect $\Gamma_v \rightarrow X_c$ fundamental bulk band gap.[5] In the ternary (also *pseudobinary*) zb-Al$_x$Ga$_{1-x}$N alloys, the electronic states, responsible for the band gaps in the pure bulk phases, intermix with respect to the relative concentration of each material component. Thus there

is a critical cation concentration that marks the transition of the fundamental alloy band gap from involving either the bulklike Γ_c conduction band states originating from the direct zb-GaN band gap or the bulklike X_c conduction band states of the indirect zb-AlN band gap. This direct-indirect band gap crossing is a common alloy characteristic of the cubic group-III nitrides and the group-III arsenides. Analogously to zb-AlN, AlAs, which naturally crystallizes in a stable zinc-blende structure, is the only indirect semiconductor among the group-III arsenides. The critical Al concentration for the direct-indirect band gap crossing in $Al_xGa_{1-x}As$ has experimentally been found at ~ 0.4.[21] A detailed knowledge of the direct-indirect band gap crossing points and accurate band gap data over the whole composition range of multicomponent semiconductor alloys is of fundamental interest for the engineering of optoelectronic and electronic devices.

The experimental band gaps of the binary bulk semiconductors zb-AlN and zb-GaN have been reported consistently in several experimental studies. The absorption/ellipsometry/reflectivity investigations of zb-AlN at room temperature (RT) yielded for the indirect $\Gamma_v \rightarrow X_c$ band gap values of 5.34 eV (see Ref. 5) and 5.3 eV (see Ref. 22) as well as of 5.93 eV (see Ref. 22) and 6.05 eV (see Ref. 23) for the direct $\Gamma_v \rightarrow \Gamma_c$ band gap. The direct $\Gamma_v \rightarrow \Gamma_c$ band gap of zb-GaN at RT was determined with 3.231 eV (see Ref. 10), 3.2 eV (see Ref. 24), 3.25 eV (see Ref. 23), and 3.232 eV (see Ref. 25), while values of 3.302 eV (see Ref. 10) and 3.295 eV (see Ref. 25) have been reported for $T = 10$ K.

For zb-$Al_xGa_{1-x}N$ alloys, the experimental data on the direct-indirect band gap crossover are limited and partially completely inconsistent with theoretical data. Okumura *et al.*[24] investigated the optical properties of molecular beam epitaxy (MBE) zb-$Al_xGa_{1-x}N$ epilayers by cathodoluminescence and spectroscopic ellipsometry techniques. Their data indicate a direct nature of the fundamental band-edge transitions over the whole composition range that is characterized by a linear increase of the alloy band gap [$E_{gap}^{zb-Al_xGa_{1-x}N}(x) = 1.6x + 3.2$ eV] with increasing Al content. Guerrero *et al.*[23] carried out room temperature reflectivity measurements on MBE grown zb-$Al_xGa_{1-x}N$ epilayers and deduced a nonlinear functional dependence [$E_{gap}^{zb-Al_xGa_{1-x}N}(x) = 6.05x + 3.25(1 - x) - 1.4x(1 - x)$ eV] of the lowest direct absorption edge on the Al concentration. Nakadaira and Tanaka[26] used near-band-edge photoluminescence spectroscopy at room temperature to investigate the zb-$Al_xGa_{1-x}N$ alloy in the Ga-rich region for $0 \leqslant x \leqslant 0.23$ and reported a linear band gap dependence [$E_{gap}^{zb-Al_xGa_{1-x}N}(x) = 1.85x + 3.2$ eV] on the Al content. All three experimental studies on zb-$Al_xGa_{1-x}N$ predict similar direct band gap transitions below $x \leqslant 0.5$. However, only the data of Guerrero *et al.* are consistent with the measured direct band gap of zb-AlN, while the data of Okumura *et al.* are neither in agreement with the direct nor the indirect band gap of zb-AlN. Guerrero *et al.* explicitly stated that there is no experimental indication for a direct fundamental absorption edge of zb-$Al_xGa_{1-x}N$ alloys. To the best of our knowledge, no experimental study has published a definitive value for the direct-indirect band gap crossing point in zb-$Al_xGa_{1-x}N$ alloys so far.

An analysis of reported theoretical data reveals inconsistencies in the numerical description of the composition dependence of the fundamental zb-$Al_xGa_{1-x}N$ band gaps as well. Recently, Amin *et al.*[27] employed the Wu-Cohen generalized gradient approximation (GGA) within a full-potential linearized augmented plane wave approach (FLAPW) to calculate the zb-$Al_xGa_{1-x}N$ band gaps over the entire composition range. Consistent with the band gap data of Okumura *et al.*, the alloy band gap was found to be direct for the entire composition range, increasing linearly from a direct band gap of 3.00 eV in zb-GaN to a direct band gap of 5.50 eV in zb-AlN. However, this result stands in disagreement with the majority of theoretical studies. Early effective pseudopotential method (EPM) studies of Fan *et al.*[28,29] reported a direct-indirect band gap crossover in zb-$Al_xGa_{1-x}N$ at $x = 0.52$. Albanesi *et al.*[30] reported a similar crossing point of $x = 0.57$ from band structure calculations applying a linear-muffin-tin-orbital (LMTO) implementation of density functional theory (DFT) in local density approximation (LDA). In this study, a cluster expansion approach (CEA)[31–33] was used to treat the problem of the stochastically occupied semiconductor alloys. Sökeland *et al.*[34] published the first GW quasiparticle (QP) theory data on zb-$Al_xGa_{1-x}N$ alloys. Their data indicate an increase of the critical Al content from $x = 0.54$ in DFT-LDA to $x = 0.63$ in the GW approximation (GWA). In both cases, the virtual crystal approximation (VCA)[33] was applied to model the semiconductor alloys. A DFT-LDA band gap crossing point of ~ 0.6 has been confirmed in further studies.[35,36] Using the screened-exchange LDA method[37–39] within DFT and special quasirandom structures (SQS's),[33,40] Lee and Wang[41] predicted the direct-indirect band gap crossing point at $x = 0.85$. Very recently, Mourad and Czycholl[42] employed an empirical tight-binding model (ETBM) to calculate the electronic structure of substitutionally disordered alloys. Besides large unit-cell (2000–4000 atoms) calculations, the disordered systems were treated within the coherent potential approximation (CPA)[43–45] and the VCA. The crossover point in zb-$Al_xGa_{1-x}N$ was found to fall into the concentration range from $x = 0.7$ to $x = 0.8$. A short summary of various theoretical studies, including the computational method and the modeling approach to treat the substitutional disorder in the Al-Ga cation sublattice is given in Table I. In light of the partially contradictory results, a

TABLE I. Theoretical data on the direct-indirect band gap crossover in zb-$Al_xGa_{1-x}N$ alloys. Listed are the approaches to describe the electronic structure and the substitutionally disordered alloy as well as the Al concentration x at the crossing point. The entries are ordered according to their time of publication.

Simulation method		Crossing	
Electronic structure	Random alloy	x	Ref.
LMTO-LDA	CEA	0.52	30
EPM	VCA	0.57	28, 29
DFT-LDA	VCA	0.54	34
GWA	VCA	0.63	34
DFT-LDA	8 atom unit cells	0.6	35
DFT-LDA	8/16 atom SQS's	0.61	41
DFT-(sX-LDA)	8/16 atom SQS's	0.85	41
DFT-LDA	8 atom unit cells	0.69	36
ETBM	CPA, VCA	0.7–0.8	42

rigorous numerical study as well as a careful investigation of zb-Al$_x$Ga$_{1-x}$N alloys by experimental techniques is needed to verify the true nature of the fundamental alloy band gap. This study serves both aspects by presenting state-of-the-art *ab initio* calculations and latest synchrotron based ellipsometry data on zb-Al$_x$Ga$_{1-x}$N over the entire concentration range.

The paper is organized as follows. Section II contains the details of the experimental setup as well as a discussion of critical points in the measured dielectric functions (DFs). In Sec. III, the key ideas of the numerical approaches, needed to calculate accurate band gaps and to model the infinite randomly occupied semiconductor alloys, are summarized. Furthermore, the application to the binary bulk materials is discussed in detail. Section IV is used for the presentation and discussion of the theoretical and experimental transition energies, while Sec. V summarizes the relevant results of this study and gives concluding comments and reasonings.

II. EXPERIMENT

A. Experimental details

For this study, epitaxial zb-Al$_x$Ga$_{1-x}$N layers spanning the full composition range were grown by plasma assisted molecular beam epitaxy. The two binary samples, zb-GaN and zb-AlN, were taken from earlier studies. Detailed reports about their optical properties and sample structures can be found elsewhere.[22,25] The zb-Al$_x$Ga$_{1-x}$N layers were grown on 3C-SiC(001)/Si substrates. The thickness of the sample layers ranges between 50 and 380 nm. Lattice parameters and Al concentration were determined by high-resolution x-ray diffraction (HRXRD). The amount of hexagonal group III-nitride inclusions have also been checked by performing reciprocal space maps (RSM) around the symmetric GaN (002) or AlN (002) reflex. From the intensity ratio of the cubic (002) reflex to the hexagonal (10$\bar{1}$1) reflex, we estimate about 99% cubic phase in both GaN and AlN samples. Further details on the structural properties are given in Refs. 46 and 13.

The linear optical response of all samples was measured by spectroscopic ellipsometry (SE) using two different setups at room temperature. In the energy range between 1 and 6.4 eV, a variable angle ellipsometer (J.A. Woollam) was used at the incidence angles of 60°, 67°, and 74°. Data up to 20 eV were recorded employing the dedicated rotating analyzer ellipsometer attached to the Berlin electron storage ring for synchrotron radiation (BESSY II). Here, the angle of incidence is fixed to 67.5° up to 10 eV and to 45° between 10 and 20 eV. Low-temperature experiments at 10 K are only possible in the range between 5 and 10 eV due to limitations of the setup. More details about the synchrotron-ellipsometer setup are published elsewhere.[47]

The ellipsometric parameters Ψ and Δ from both setups and all angles of incidence were merged and fitted by taking into account the layer structure, surface and interface roughnesses of the respective sample yielding the complex DF $\varepsilon(\hbar\omega) = \varepsilon_1(\hbar\omega) + j\varepsilon_2(\hbar\omega)$. As ε_1 and ε_2 are related by the Kramers-Kronig relations, it is sufficient to present either one. Here, we show the imaginary part of the DFs, ε_2.

B. Experimental results

The imaginary parts of the DFs at room temperature are presented in Fig. 1. Note that for three of our samples ($x = 0.26$, 0.50, and 0.71), only data up to 10 eV are available. At the low-energy side, each sample shows an absorption onset, i.e., a steplike behavior of ε_2 marking the energy position of the direct band gap. While the steps are relatively sharp for the two binary compounds, the ternary alloy films show larger broadenings of the onset. This behavior is expected already from statistical disorder in the randomly distributed cation matrix containing Al and Ga atoms in a certain fraction but with locally different concentrations. The large broadening and the low layer thicknesses do not allow to determine the indirect band gaps in this composition range. However, as demonstrated previously for zb-AlN[22] and zb-GaN,[25] accurate values for the $\Gamma_v \rightarrow \Gamma_c$ spacing (band gap E_0) can be determined from the analysis of the ε_2 data by taking the excitonic effects around the absorption edge into account yielding for the two binaries 5.93 and 3.232 eV, respectively. The obtained E_0 values of all samples are summarized in Fig. 2.
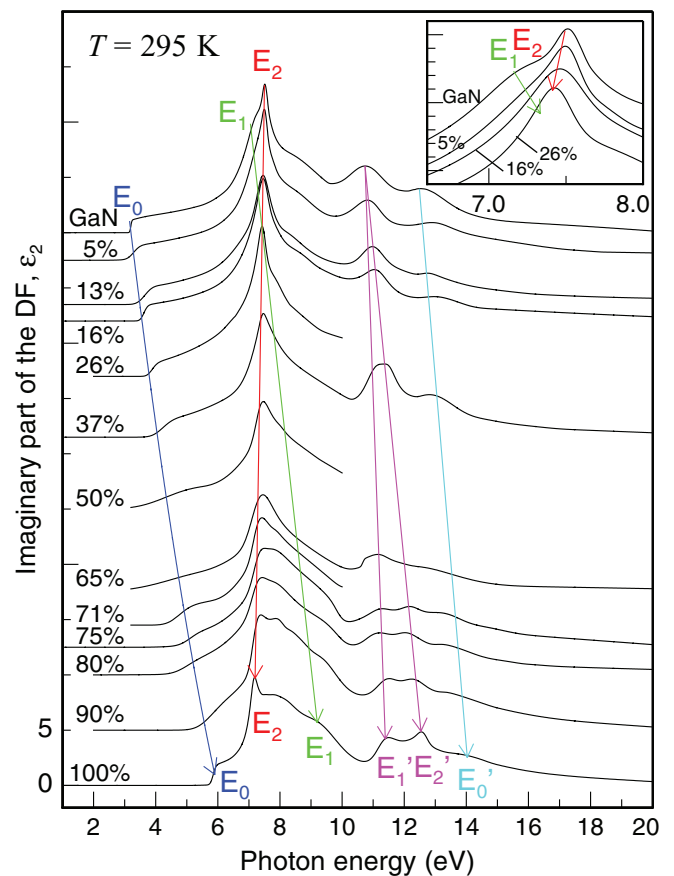

FIG. 1. (Color online) Imaginary parts (ε_2) of the complex dielectric function of the zb-Al$_x$Ga$_{1-x}$N samples up to 20 eV measured at room temperature (295 K). The spectra are shifted vertically for clarity proportional to their gallium content [$\times 50(1-x)$]. The connecting continuous curves are guidelines for the eye and mark absorption transitions occurring at the same point in the Brillouin zone. The inset presents details around the E_2 contribution for low aluminum content samples. It can be clearly seen that E_2 shifts to lower energy for increasing Al concentration.
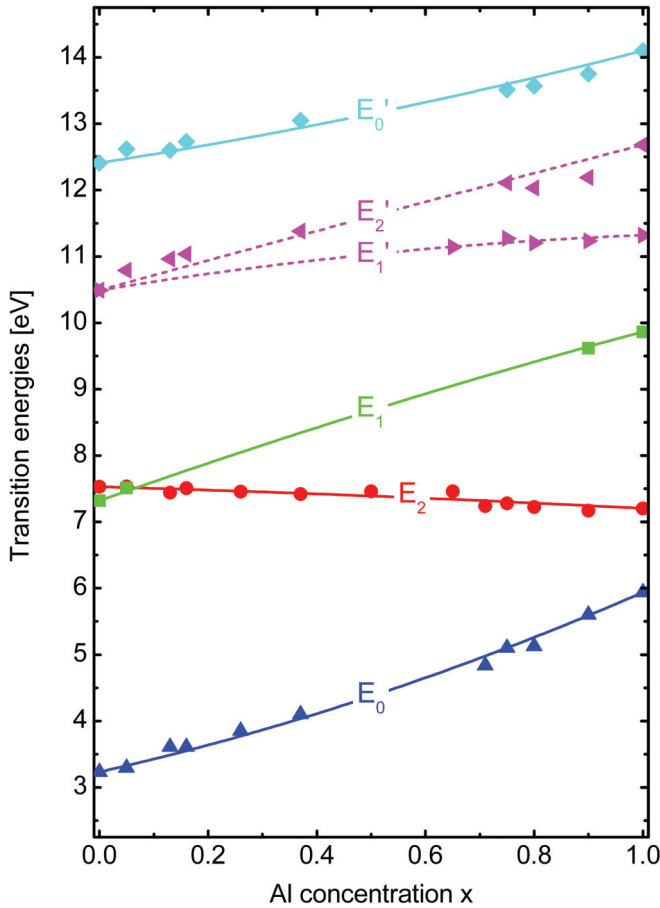
FIG. 2. (Color online) Characteristic transition energies as obtained from analysis of critical points in the measured dielectric functions of zb-Al$_x$Ga$_{1-x}$N at room temperature (295 K) as a function of the aluminum concentration x.

A couple of characteristic high-energy features are found in all spectra, their dependence on the alloy content are indicated by continuous lines in Fig. 1. Except for E_2, all characteristic transitions shift to higher energies for increasing Al concentration. This behavior is analogous to that of wz-Al$_x$Ga$_{1-x}$N alloys[48] where also only one feature is shifting to smaller energy for an increasing Al content. The most prominent feature in ε_2 is visible at around 7.5 eV for all samples. This sharp peak (E_2) has already been successfully identified with the interband absorption at the X point of the Brillouin zone in zb-AlN[22] and zb-GaN.[25] A more detailed analysis of this peak reveals that it shifts from 7.51 eV for zb-GaN to 7.204 eV for zb-AlN. The inset in Fig. 1 displays a closer look of the behavior of E_2 for the low Al content samples. In the direct vicinity of E_2 in the spectra we find a feature labeled E_1, which is below the E_2 contribution for zb-GaN (at 7.23 eV) but above E_2 for zb-AlN (at 9.8 5eV). We identify this band by interband absorption at the Λ line between the L and Γ points of the zinc-blende Brillouin zone in agreement with earlier studies.[25,49] At even higher energies we find two separate contributions for zb-GaN at 10.72 and 12.87 eV, while in zb-AlN these contributions are split into three peaks at 11.32, 12.68, and 14.1 eV. We label them E_1', E_2', and E_0', respectively. The prime marks interband transitions

into higher conduction bands at the same point in the Brillouin zone.

In order to allow a comparison of these experimental transition energies with the results of the band structure calculations, the influence of electron-hole interaction (excitonic effects) on the shape of ε_2 in the vicinity of high-energy critical points has to be considered. A detailed discussion for zb-AlN has been published recently where the shape of the independent-quasiparticle DF (disregarding electron-hole many-body interaction) and the excitonic DF as obtained by solving the Bethe-Salpeter equation was analyzed.[49] In particular, a pronounced feature related to E_2 becomes only visible by the inclusion of excitons (inset of Fig. 6 in Ref. 49). It peaks at 7 eV, while the corresponding quasiparticle gap amounts to 7.22 eV. Conversely, by adding the 220 meV difference to the experimental E_2 value reported above one obtains 7.424 eV for the quasiparticle gap at the X point. The size of the shift has not been calculated yet for the alloys, i.e., we cannot correct the whole curve in Fig. 2. However, a pronounced change of the correction value is unlikely because the transition energy undergoes only a 300 meV upshift with decreasing Al content. Correspondingly, the excitonic-induced downshift for E_2' amounts to 300 meV, while other transitions cannot be unambiguously identified in the calculated DF.[49]

In order to quantify the nonlinear deviations of the alloy band gaps, the bowing parameters $b_\mathbf{k}$ were determined according to

$$E_{\text{gap},\mathbf{k}}^{\text{Al}_x\text{Ga}_{1-x}\text{N}} = E_{\text{gap},\mathbf{k}}^{\text{AlN}} x + E_{\text{gap},\mathbf{k}}^{\text{GaN}}(1-x) - b_\mathbf{k} x(1-x). \quad (1)$$

The k-point index indicates that the electronic states of the alloy are labeled by the symmetry of their equivalents in the individual bulk materials. Positive and negative bowing parameters indicate a downward and upward bowing, respectively, with respect to a linear dependence on the alloy composition. The fundamental direct band gap (E_0) can be described by a nonlinear interpolation including a notable downward bowing characterized by a bowing factor of $b_\Gamma = 0.85$ eV. In general, other high-energy critical-point energies also show a nonlinear dependence on the Al concentration as discussed below. Theoretical first-principles calculations as presented below are usually performed for zero temperature. It is thus appropriate to consider the influence of sample temperatures on the energy positions of the features in the DFs. Therefore we have performed low-temperature (10 K) synchrotron spectroscopic ellipsometry experiments for the binary components zb-GaN and zb-AlN. While the data for zb-GaN were already published earlier,[25] these for zb-AlN are presented in Fig. 3. For 10 K, we find decreasing broadening and increasing amplitude of high-energy features in the DF. Furthermore, the whole DF is shifted to higher energy values due to reduced electron-phonon interaction. E_2 is located at 7.271 eV for 10 K, which resembles an upshift of 67 meV. The shift of E_0 is found to be similar. The corresponding shifts were found to be 63 meV (E_0) and 110 meV (E_2) for zb-GaN (see Ref. 25). It is therefore reasonable to estimate the temperature shift from 295 to 10 K for all features in ε_2 to about 100 meV for the whole alloy system. When comparing calculated quasiparticle band energies to experimentally obtained transitions as done below, this shift should be kept in mind.
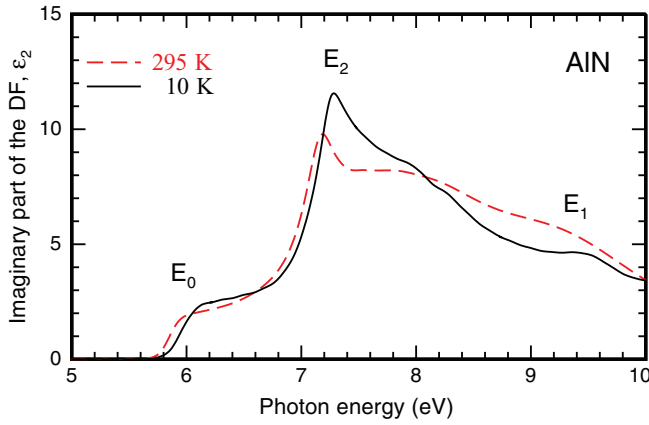
FIG. 3. (Color online) Imaginary parts of the dielectric functions (ε_2) of the zb-AlN samples up to 10 eV at 295 and 10 K.

In order to determine the Al concentration at the direct-indirect crossing the direct E_2 transition energies at the X point need to be aligned by the relative difference of the highest X point valence states and the position of the highest Γ point valence state (zero point of the energy scale). Since the accurate calculation of the valence band position is crucial to obtain the band gap crossing concentration, we will first discuss the suitability of various numerical approaches to simulate the electronic structure of nitride semiconductors before returning to the direct-indirect band gap crossing in Sec. IV.

III. THEORY

A. *Ab initio* calculations

The theoretical determination of the direct-indirect band gap crossing necessitates both a highly precise description of all extremal points of the band structure and an accurate reproduction of the infinite randomly occupied semiconductor alloy over the entire composition range.

Nowadays, the Kohn-Sham formulation[50] of DFT[51] is practically established as a standard for atomistic calculations in the solid-state community. The interpretation of energy differences between Kohn-Sham ground-state eigenvalues,[52] obtained using either the LDA[53–55] or the GGA[56–59] to approximate the exchange-correlation (XC) potentials and energies, as excitation energies has resulted in severely underestimated, unsatisfying band gap energies for a vast majority of semiconductors and insulators or even absent band gaps for small-gap systems (e.g., Ge, GaSb, and InAs, see Ref. 60). This so-called *band gap problem* is commonly portrayed as the most prominent unsolved problem of DFT and handicaps the communication of numerical results to nonspecialist readers less familiar with the theoretical foundations of DFT. The origin of the band gap underestimation can be traced back to self-interaction errors as well as the lack of a derivative discontinuity at integer electron number in approximated XC functionals.[52,60–65] The accuracy of conventional (semi)local DFT is often still sufficient to provide a sound basis for qualitative and quantitative interpretation of experimental data and, beyond that, it even shows some degree of inherent predictive power. Nevertheless, much methodological work in electronic structure theory has been devoted to the band gap

problem in DFT. From a theoretical point of view, the focus of this study is to go beyond conventional DFT and apply various electronic structure methods, including many-body perturbation theory (MBPT),[66,67] that can be expected to give more accurate band gap values.

(1) TB-mBJLDA: Recently, Tran and Blaha[68] proposed an in-real-space multiplicative Kohn-Sham-like potential by modifying the Becke-Johnson (BJ) exchange potential[69,70]

$$v_{x,\sigma}^{\mathrm{TB\text{-}mBJ}}(\mathbf{r}) = c\, v_{x,\sigma}^{\mathrm{BR}}(\mathbf{r}) + (3c-2) \frac{1}{\pi}\sqrt{\frac{5}{12}}\sqrt{\frac{2t_\sigma(\mathbf{r})}{\rho_\sigma(\mathbf{r})}}, \quad (2)$$

where

$$v_{x,\sigma}^{\mathrm{BR}}(\mathbf{r}) = -\frac{1}{b_\sigma(\mathbf{r})}\left[1 - e^{-x_\sigma(\mathbf{r})} - \frac{1}{2}x_\sigma(\mathbf{r})\, e^{-x_\sigma(\mathbf{r})}\right] \quad (3)$$

is the Becke-Roussel exchange potential[71] as proposed earlier to model the Coulomb potential created by the exchange hole. Here, $\rho_\sigma = \sum_{i=1}^{N_\sigma}|\psi_{i,\sigma}|^2$ and $t_\sigma = (1/2)\sum_{i=1}^{N_\sigma}(\nabla\psi_{i,\sigma}^* \cdot \nabla\psi_{i,\sigma})$ are the electron and kinetic-energy densities, x_σ is determined from a nonlinear equation containing t_σ as well as the density gradients $\rho_\sigma, \nabla\rho_\sigma$, and $\nabla^2\rho_\sigma$, and b_σ are calculated according to $b_\sigma = [x_\sigma^3\, e^{-x_\sigma}/(8\pi\rho_\sigma)]^{1/3}$. Equation (2) ensures that for any value of c the LDA exchange potential is approximately recovered for a constant electron density. For $c=1$ the original BJ potential is recovered. The actual value of the c parameter in Eq. (2) is calculated from the cell average of the quantity $|\nabla\rho/\rho|$ via

$$c = \alpha + \beta\left[\frac{1}{V_{\mathrm{cell}}}\int_{\mathrm{cell}}\frac{|\nabla\rho(\mathbf{r}')|}{\rho(\mathbf{r}')}d^3r'\right]^{1/2}, \quad (4)$$

where V_{cell} is the unit-cell volume and α and β are two free parameters, whose values ($\alpha = -0.012$, $\beta = 1.023$ bohr$^{1/2}$) are determined to minimize the mean absolute relative error of the band gap for a representative set of solids (see Ref. 68). Due to their dependence on the kinetic energy density t_σ, the exchange potentials above can be classified as meta-GGA's. In practical calculations, the TB-mBJ exchange potential is used in combination with an LDA correlation potential[55] (TB-mBJLDA). Since the TB-mBJ exchange potential cannot be obtained as a functional derivative ($\delta E_{\mathrm{xc}}[\rho]/\delta\rho$) of the total energy,[72] it is not possible to use the TB-mBJLDA potential for force calculations. Thus structure relaxations have to be done using alternative XC functionals.

The TB-mBJLDA potential has been shown to reproduce experimental band gaps with an error margin of the same order as hybrid functional or GW approaches (see Ref. 68), thereby preserving the moderate computational cost of conventional DFT. In principle, the TB-mBJLDA method can be seen as a parameter-free approach, since the c parameter can be calculated self-consistently according to Eq. (4). However, using the self-consistently estimated values of c electronic band gaps in semiconductors and insulators tend to be underestimated.[73–75] Since band gaps typically show a monotone increase with increasing c,[68] c can be adjusted manually to match the experimental band gaps. In a study on band structure topologies of III-V semiconductors, Kim *et al.*[73] reported an excellent TB-mBJLDA description of band gaps at high-symmetry points, although a general overestimation of effective masses by 20–30% was reported.

Recently, Kresse *et al.*[75] demonstrated that fundamental band gap energies obtained with the TB-mBJLDA potential and a properly adjusted c parameter can even compete with the most sophisticated self-consistent GW schemes. However, a significant tendency toward to narrow bandwidth and consequentially a nonadequate representation of the optical response was reported by using TB-mBJLDA orbitals to solve the Bethe-Salpeter equation.

(2) LDA-1/2: Another approach to improve the description of band gaps by approximately taking into account self-energy corrections within the framework of conventional Kohn-Sham DFT in LDA is the LDA-1/2 half-occupation technique. LDA-1/2 has been derived in the spirit of Slater-Janack transition-state theory[76–78] and was recently developed by Ferreira *et al.*[79,80] into a practical scheme for band gap calculations of semiconductors. While the half-occupation scheme provides accurate atomic ionization potentials,[79] it cannot be directly applied to extended crystalline systems. In the LDA-1/2 approach the orbital-dependent self-energy

$$S_\alpha = \int n_\alpha (\mathbf{r}) \, V_S (\mathbf{r}) \, d^3 r \qquad (5)$$

of a Kohn-Sham state α with electron density $n_\alpha (\mathbf{r})$ is subtracted from the Kohn-Sham eigenvalue at full occupation. Therefore the self-energy potential V_S, is approximately given as the difference

$$V_S \approx -V(-1/2, r) + V(0, r) \qquad (6)$$

between the all-electron potentials of an atom and its half-ion. V_S has been interpreted as the work required to transform the charge of a Bloch function into a localized hole state.[81] In crystals, the self-energy correction is added to the atomic (pseudo)potentials of all atoms, thus calculating the properties of a "filled hole band" instead of individual localized hole states. To avoid the penetration of the self-energy Coulomb tails into neighboring atom sites, the self-energy potentials are trimmed according to $V_S' = \theta(r) V_S$ by a cutoff function $\theta(r)$:

$$\theta (r) = \begin{cases} \left[1 - \left(\frac{r}{\text{CUT}} \right)^{n=8} \right]^3 & r \leqslant \text{CUT}, \\ 0 & r > \text{CUT}. \end{cases} \qquad (7)$$

Ideally, LDA-1/2 can be considered to be fully *ab initio*, since the value of the CUT parameter is determined in a variational way to make the band gaps extremal without falling back to empirical parameters. If not stated otherwise, the LDA-1/2 results, presented throughout this study, are obtained by adding self-energy correction potentials with a cutoff of CUT = 2.90 a.u. to the N_{2p} states in zb-AlN and zb-GaN. For zb-GaN, additional self-energy corrections with a cutoff of CUT = 1.15 a.u. have been included for the Ga_{3d} states.

LDA-1/2 has led to very impressive band gap results[79] for a large number of materials ranging from small-gap semiconductors to wide-gap semiconductors and insulators. Thereby, LDA-1/2 even surpasses non-self-consistent GWA approaches[82,83] and partially or fully self-consistent GW approaches that neglect the influence of electron-hole vertex corrections (cf. Ref. 84). The LDA-1/2 approach was recently used by Pelá *et al.*[85] to model the band gaps of the ternary group-III nitride alloys wz-$Al_x Ga_{1-x}$N, wz-$In_x Ga_{1-x}$N, and wz-$Al_x In_{1-x}$N. The LDA-1/2 band gaps were found to fit

remarkably well with the experimental results for all studied alloys. Using the example of polar and nonpolar InN surfaces Belabbes *et al.*[86] demonstrated that the LDA-1/2 method allows an approximate computation of accurate QP excitations, that are on the same level as combined hybrid functional and GW results, even for extended surface systems. Further examples of LDA-1/2 studies include the electronic bands and their alignment in various III-V semiconductors and their polytypes,[87] the energetics of SnO_2 surfaces,[88] and the band offsets at AlAs/GaAs and $Al_x Ga_{1-x}$As/GaAs interfaces[89] as well as Si/SiO_2 interfaces.[81] In a nutshell, the LDA-1/2 method provides a promising approach for an approximate description of QP characteristics of the electronic-structure of large scale semiconductor and insulator structure models at the computational cost of conventional (semi)local DFT.

(3) HSE: An alternative approach to an accurate, DFT-based band-structure description is the use of nonlocal, nonmultiplicative XC potentials to solve a generalized eigenvalue problem that formally lies outside the KS framework.[37,38] Especially nonlocal hybrid functionals, which replace some fraction of (semi)local DFT exchange by (Hartree-)Fock (also exact) exchange energy (e.g., PBE0[59,63,90,91]), have been applied quite successfully in solid state theory. Thereby the inclusion of an exact-exchange interaction fraction ($\sim 25\%$) is not only motivated by the observation of reverse band gap errors in (semi)local DFT and Hartree-Fock (HF) theory, but also rationalized by theoretical considerations.[92] A class of modern, extensively applied, hybrid functionals are HSE (Heyd-Scuseria-Ernzerhof) functionals[60,93–95] that restrict the inclusion of exact Fock exchange E_X^{HF} to short-range contributions. In general, the long-range (LR) exchange interaction and the correlation energy E_c remain unchanged with respect to the PBE functional (E_X^{PBE} and E_C^{PBE}), therefore, a HSE-type functional exhibits the form

$$\begin{aligned} E_{\text{XC}}^{\text{HSE}} = {} & \alpha E_X^{\text{HF,SR}} (\mu) + (1 - \alpha) E_X^{\text{PBE,SR}} (\mu) \\ & + E_X^{\text{PBE,LR}} (\mu) + E_C^{\text{PBE}}. \end{aligned} \qquad (8)$$

Thereby the range separation into LR and short-range (SR) parts of E_X^{HF} is carried out by a decomposition of the Coulomb kernel according to

$$\frac{1}{r} = \underbrace{\frac{erfc(\mu r)}{r}}_{\text{SR}} + \underbrace{\frac{erf(\mu r)}{r}}_{\text{LR}}. \qquad (9)$$

The parameter α defines the percentage of exact Fock exchange. In agreement with the original definitions,[93–96] we refer to the parameter values $\alpha = 0.25$, $\mu = 0.2$ Å^{-1} as HSE06. The screening parameter μ is not changed throughout this work. However, since a fixed amount of exact exchange and a nonvariable screening limit the flexibility of the HSE06 functional, it is a common practice (especially for wide-gap materials[20]) to sacrifice the essence of *ab initio* theory by searching material optimized values for α and μ.

In general, the use of HSE-type hybrid functionals has shown significant improvements in the description of electronic band gaps,[60,97–100] band offsets,[20,101] defect levels,[102–104] and the prediction of accurate direct-indirect band gap crossovers.[101] Nevertheless the gain of accuracy increases the

computational cost by two orders of magnitude compared to conventional (semi)local DFT.

(4) GW: The final approach applied in this study to include many-particle interactions beyond Kohn-Sham-like single-particle mean-field theories is based on MBPT, as formulated by Hedin.[66,67] MBPT formally recast the solution of the *electronic-structure problem* into a closed fundamental system of five coupled integral equations for the Greens function G, the screened Coulomb interaction W, the self-energy Σ, the polarization propagator P, and a vertex function Γ. Due to the complicated nature of the functional dependence of $\Sigma = \Sigma[G]$ on G, Hedin's equations have to be solved self-consistently. In practice, these equations are decoupled by narrowing the vertex corrections to zeroth order as originally proposed by Hedin[67] (i.e., GWA). Within GWA, the energies $E_{n\mathbf{k}}^{\mathrm{QP}}$ of single excited (quasi)electrons and (quasi)holes, as experimentally accessible in direct and inverse photoemission spectroscopy experiments, are obtained as solutions to a set of nonlinear differential equations,[67,105] that are found to be similar to the Kohn-Sham equations:

$$\left(T + V_{\mathrm{ext}} + V_H - \varepsilon_{n\mathbf{k}}^{\mathrm{QP}}\right)\Psi_{n\mathbf{k}}(\mathbf{r})$$
$$+ \int d^3\mathbf{r}' \Sigma\left(r, r', \varepsilon_{n\mathbf{k}}^{\mathrm{QP}}\right)\Psi_{n\mathbf{k}}(\mathbf{r}') = 0. \qquad (10)$$

Here, the Kohn-Sham XC functional $V_{xc}^{\mathrm{KS}}(r)$ is replaced by the nonlocal energy-dependent self-energy operator $\Sigma(r, r', \varepsilon_{n\mathbf{k}}^{\mathrm{QP}})$ that carries the information of the many-body interactions. The GWA self-energy, given to first order in W, is evaluated as a convolution integral of the single-particle Greens function G and the dynamically screened Coulomb interaction W,

$$\Sigma(r, r', \omega) = \frac{i}{4\pi}\int_{-\infty}^{\infty} d\omega' e^{i\omega'\delta} G(\mathbf{r}, \mathbf{r}', \omega + \omega') W(\mathbf{r}, \mathbf{r}', \omega').$$
$$(11)$$

Here, δ is a infinitesimal positive number. In the most common GWA calculations, DFT eigenvalues and wave functions are used as input for the calculation of QP energy correction within a first-order perturbation theory approach (i.e., G_0W_0). The first-order energy corrections (so-called QP shifts) $\Delta\varepsilon_{n\mathbf{k}}^{\mathrm{QP}}$ are given by

$$\Delta\varepsilon_{n\mathbf{k}}^{\mathrm{QP}} = Z_{n\mathbf{k}}\,\mathrm{Re}\left\langle\Psi_{n\mathbf{k}}^{\mathrm{KS}}\middle|\Sigma\left(\varepsilon_{n\mathbf{k}}^{\mathrm{KS}}\right) - V_{xc}^{\mathrm{KS}}\middle|\Psi_{n\mathbf{k}}^{\mathrm{KS}}\right\rangle, \qquad (12)$$

where the perturbation is given by the difference between the self-energy and the DFT XC functional and $Z_{n\mathbf{k}}$ represents a renormalization factor.[38,105–107] G_0W_0 calculations systematically improve the DFT band gaps.[83,108,109] However, this perturbative approach shows a strong dependence on the choice of the initial wave functions that can be taken from (semi)local DFT, hybrid functional DFT or other approaches.[20,38,110] Effects of self-consistency within the GW approach are considered partially by repeated calculation of QP corrections with updated QP eigenvalues in G or both G and W.[38,107] The according approaches are known as, GW_0 and GW. For numerous semiconductors, GW_0 QP energies are very close to experimental results.[83,107] Nevertheless, QP corrections in the various self-consistent approaches do not necessarily improve the band gap description over the computationally less demanding non-self-consistent G_0W_0 approaches. Especially the fully self-consistent GW QP energies tend to overestimate

the experimental values for electronic band gaps.[38,83] Aside from self-consistency with respect to QP energies, also the one-electron orbitals, initialized by various choices of Kohn-Sham DFT orbitals, may be updated self-consistently.[82,84,111] Again, updated QP energies and one-electron orbitals may be considered in the Green function G only (i.e., scGW_0) or in G and the screened Coulomb potential W (i.e., scGW). Since improvement over *single shot* G_0W_0 with carefully selected initial DFT one-electron orbitals are sparse in the self-consistency schemes above, it has been stated that the inclusion of an attractive electron-hole interaction (i.e., vertex corrections) might be the next systematic improvement over the various GW schemes applied hitherto.[75,84,112] In practice, even non-self-consistent G_0W_0 calculations show a prohibitive computational cost for larger unit cells of, e.g., surfaces or alloys by even surpassing the computational demands of hybrid-functional approaches.

Obviously, a detailed knowledge of the performance of the approaches above with respect to various material characteristics is of fundamental interest. In particular, given that the computational expense of these approaches increases from standard (semi)local DFT equivalent cost by two to three orders of magnitude in case of hybrid-functional DFT or the even more sophisticated GW QP theories.

B. Alloy modeling

In order to simulate the substitutional disorder of the ternary semiconductor compounds, we adopted two different strategies both aiming at an adequate *single* unit-cell representation of the alloys. On the one hand, we generated cubic 8, 64, and 216 atom unit cells (labeled by RAND) with randomly occupied cation sublattices to study the influence of the artificially introduced system size dependent periodicity errors. We compare these arbitrary representations of the random alloys to special quasirandom structures (SQSs) constructed according to Zunger (see Refs. 33 and 40). A SQS is designed to mimic the structural correlations of the perfectly random alloy as closely as possible within the most relevant lowest order structure correlations. Thereby the basic assumption of the SQS approach is that most physical properties show a hierarchical dependence on the interaction distance with clearly dominating short-range (pair) correlations and negligible pair and multisite correlations at larger distances. For details on the generation of SQSs, we refer the reader to the numerous literature.[33,40,45] SQSs, with just a few atoms per unit cell, promise to keep the required resources of the more elaborate computational schemes within reasonable limits and to circumvent the problem of scanning a large number of different lattice configurations to utilize statistical approaches. Nevertheless, it is worth to note that alloys are best described by statistical averages on sufficiently extended unit cells. Ultimately, an answer to the basic question if a single unit-cell-based approach can be sufficient to characterize stochastic substitutional disorder in an semiconductor alloy will be closely connected to its chemical composition. In particular, the extend of the lattice mismatch between the individual material components and the degree of local atomic relaxations, will be significant. So far, SQSs have been successfully applied to calculate the spatial and electronic structures
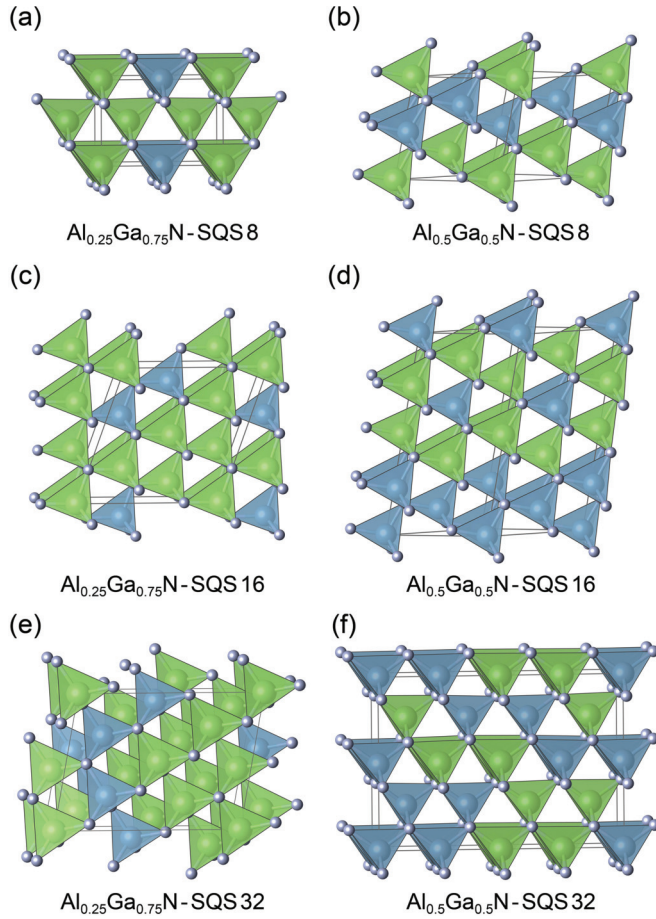
(a) Al$_{0.25}$Ga$_{0.75}$N-SQS 8

(b) Al$_{0.5}$Ga$_{0.5}$N-SQS 8

(c) Al$_{0.25}$Ga$_{0.75}$N-SQS 16

(d) Al$_{0.5}$Ga$_{0.5}$N-SQS 16

(e) Al$_{0.25}$Ga$_{0.75}$N-SQS 32

(f) Al$_{0.5}$Ga$_{0.5}$N-SQS 32

FIG. 4. (Color online) Polyhedra representation of 8, 16, and 32 atom SQS's unit cell for ternary zb-Al$_x$Ga$_{1-x}$N alloys. Tetrahedral AlN$_4$ units are displayed in blue and GaN$_4$ units in green. For zb-Al$_{0.75}$Ga$_{0.25}$N, the chemical elements of the zb-Al$_{0.25}$Ga$_{0.75}$N cation sublattice are interchanged. For each SQS, the particular unit cell is draw as grey lines. The illustrations have been done using VESTA.[113]

of various binary and multicomponent alloys.[38,114–119] An automated SQSs generation tool is provided by the alloy theoretic automated toolkit (ATAT).[120]

Our generated SQSs with 8, 16, and 32 atoms for Al concentrations of $x = 0.25$ and 0.5 are displayed in Fig. 4. The SQSs for $x = 0.75$ are obtained by interchanging the chemical elements of the zb-Al$_{0.25}$Ga$_{0.75}$N SQS's cation sublattices. Details on the SQS unit cells are given in Table II. For all

TABLE II. Details on the basic shape of the generated zb-Al$_x$Ga$_{1-x}$N SQS unit cells. The lattice vectors are given in units of $a_{\text{zb-Al}_x\text{Ga}_{1-x}\text{N}}/2$ with linearly interpolated alloy lattice constant according to Eq. (13).

Model	x	Lattice vectors		
SQS 8	0.25/0.75	(0, −1, −1)	(−2,0,0)	(0,2, −2)
SQS 8	0.5	(−2, −1, −1)	(−1, −1, −2)	(1, −2,1)
SQS 16	0.25/0.75	(−2,2, −2)	(2,2,2)	(1,0, −1)
SQS 16	0.5	(2,1, −1)	(1,1, −2)	(−2,4,2)
SQS 32	0.25/0.75	(1,1, −2)	(0, −3, −1)	(−4,1, −1)
SQS 32	0.5	(0, −1, −1)	(−4,0,0)	(0,4, −4)

composition ratios the local atomic relaxations are considered by separate relaxations of the atomic structure.

To ensure consistency throughout the different numerical approaches, all bulk calculations are performed at the experimental zb lattice constants[121,122] ($a_{\text{zb-AlN}} = 4.38$ Å, $a_{\text{zb-GaN}} = 4.52$ Å). In view of the small lattice mismatch (∼3%) of the zb-AlN and zb-GaN bulk, the zb-Al$_x$Ga$_{1-x}$N alloys are constructed assuming a linear Al concentration dependent lattice constant $a(x) = x\,4.52 + (1 − x)4.38$ Å following Vegard's law,

$$a_{\text{zb-Al}_x\text{Ga}_{1-x}\text{N}} = x\,a_{\text{zb-AlN}} + (1 − x)a_{\text{zb-GaN}}. \qquad (13)$$

The validity of Vegard's law for group-III nitride alloys has been confirmed experimentally[123] for wz-Al$_x$Ga$_{1-x}$N and in several theoretical studies on zb-Al$_x$Ga$_{1-x}$N.[35,36,124] In all structure models, local atomic relaxations were considered at the DFT-GGA level applying the Perdew-Becke-Ernzerhof (PBE)[59] XC functional and a force convergence criterion of 0.005 eV/Å.

C. Numerical details

The DFT and *GW* calculations of this study were performed using the Vienna *ab initio* simulation package (VASP) implementations.[38,83,84,107,125] An energy cutoff of 400 eV was used throughout this work to expand the Kohn-Sham orbitals into plane wave basis sets. The electron-ion interaction was described by the projector-augmented wave (PAW) method.[126,127] Throughout this work the Ga$_{3d}$ semicore states were treated as valence states in the PAW potentials. The *GW* calculations for primitive bulk unit cells of zb-AlN and zb-GaN were carried out with 256 electronic bands and 160 frequency grid points for sampling the dielectric function. In all partially or fully self-consistent *GW* calculations, the one-electron energies and optionally the one-electron orbitals have been updated eight times to reach QP band gaps that are converged within an accuracy of 0.01 eV. If not stated otherwise, the Brillouin zone integration of primitive unit cells was performed using regular Γ-centered $8 \times 8 \times 8$ k-point meshes. This again guarantees the convergence of bulk QP band gaps within 0.01 eV. In all electronic band-structure calculations the high-symmetry lines were sampled by 100 k points. Further details on the parameters used in TB-mBJLDA und HSE calculations as well as further details on the LDA-1/2 scheme as well as the *GW* approaches are given below. The Brillouin zone integration for zb-Al$_x$Ga$_{1-x}$N alloys was performed by regular Γ-centered $8 \times 8 \times 8$ and $3 \times 3 \times 3$ k-point sets for cubic 8 and 64 atom unit cells. For cubic 216 atom unit cell, the calculations were restricted to the Γ point only. For the more complicated SQS unit cells the k-point mesh was chosen to match a comparable point density in the reciprocal space.

All numerical simulations of this study do not include effects of spin polarization. Without saying, the experimental transition energies reflect the splitting due to spin-orbit interaction that is neglected in our calculations. Therefore we will not make use of explicit electronic state symmetry labels in the discussion of theoretical and experimental results. For a detailed discussion of the valence-band splitting due to spin-orbit coupling in binary group-III bulk nitrides see Refs. 128 and 129.

TABLE III. Calculated band gaps of zb-GaN and zb-AlN. Experimental data are taken from Ref. 22 for the direct and indirect band gaps of zb-AlN and from Ref. 25 for the direct band gap of zb-GaN. TB-mBJLDA results are given for two optimized c-parameter values. TB-mBJLDA* and TB-mBJLDA** refer to c parameters of $c = 1.45$ and 1.55. For modified HSE calculations, the fraction (α) of exact exchange is given. In partially and fully self-consistent GW calculations, the QP eigenvalues have been updated eight times. In the scGW_0 and scGW schemes, also updates of the one-electron orbitals have been included in the self-consistency cycle. The relative errors of the calculated band gaps with respect to the experimental values are visualized in Fig. 5. All band gap values are given in eV.

| Method | zb-AlN | | zb-GaN |
	$(\Gamma_v \rightarrow X_c)$	$(\Gamma_v \rightarrow \Gamma_c)$	$(\Gamma_v \rightarrow \Gamma_c)$
LDA	3.22	4.15	1.68
PBE	3.31	4.12	1.66
TB-mBJLDA* ($c = 1.45$)	5.40	5.78	2.99
TB-mBJLDA** ($c = 1.55$)	5.79	6.09	3.29
LDA-1/2	5.34	5.87	3.31
HSE06	4.56	5.50	2.92
mod(32)HSE ($\alpha = 0.32$)	4.92	5.90	3.30
mod(39)HSE ($\alpha = 0.39$)	5.29	6.30	3.69
G_0W_0@PBE	4.59	5.64	2.92
G_0W_0@HSE06	5.16	6.25	3.47
GW_0@PBE	5.09	6.04	3.03
GW@PBE	5.57	6.53	3.37
scGW_0@PBE	5.47	6.25	3.34
scGW@PBE	5.42	6.30	3.71
exp	5.3 (295 K)	5.9 (295 K)	3.3 (10 K)

D. Band gaps of zb-AlN and zb-GaN

In order to find an accurate description of the zb-Al$_x$Ga$_{1-x}$N alloys, we start our discussion of the numerical approaches by a comparison of the zb-AlN and zb-GaN bulk-band structure characteristics. In Table III, the absolute values of the fundamental direct and indirect energy transitions are summerized for both materials. Additionally, Fig. 5 visualizes the relative percentaged band gap errors ($E_{\mathrm{gap}}^{\mathrm{calc}} - E_{\mathrm{gap}}^{\mathrm{exp}})/E_{\mathrm{gap}}^{\mathrm{exp}} \times 100$ for all approaches.

The use of the LDA and the semilocal PBE functional yields quite similar band gaps. For both semiconductors, the calculated (semi)local band gaps show the expected characteristic underestimation. In case of zb-AlN, the direct band gap is underestimated by $\sim$39% and the indirect band gap by $\sim$30%. For zb-GaN, this underestimation actually increases to almost 50%. Larger differences between DFT-LDA and DFT-PBE results, occasionally reported, might arise from the differences in the equilibrium lattice constants of zb-AlN and zb-GaN.

The use of the TB-mBJLDA potential to calculate band gap energies drastically increases the BGs towards their experimental size. However, self-consistently determined c parameters (not listed in Table III) of $c_{\text{zb-AlN}} = 1.29$ and $c_{\text{zb-GaN}} = 1.33$ still show notably underestimated band gaps of $E_{\mathrm{gap}}^{\text{zb-AlN}}(\Gamma_v \rightarrow X_c) = 4.81$ eV, $E_{\mathrm{gap}}^{\text{zb-AlN}}(\Gamma_v \rightarrow \Gamma_c) = 5.25$ eV, and $E_{\mathrm{gap}}^{\text{zb-GaN}}(\Gamma_v \rightarrow \Gamma_c) = 2.66$ eV. This tendency has already been reported earlier.[73,75] The TB-mBJLDA band gap increases monotonically with increasing the c parameter, and c can thus be adjusted separately for each material. The optimal

choice of c for zb-GaN is $c \approx 1.55$ (labeled as TB-mBJLDA**) to reproduce the experimental band gap. For the same value of c the zb-AlN band gaps are overestimated by $\sim$9% and $\sim$3% for the indirect and direct band gaps. In case of zb-AlN we searched for a c parameter that equally improves the indirect and direct band gap. For $c \approx 1.45$ (labeled as TB-mBJLDA*), we obtain band gaps of $E_{\mathrm{gap}}^{\text{zb-AlN}}(\Gamma_v \rightarrow X_c) = 5.40$ eV and $E_{\mathrm{gap}}^{\text{zb-AlN}}(\Gamma_v \rightarrow \Gamma_c) = 5.78$ eV. The error for both zb-AlN band gaps is below $\sim$2%. Nevertheless, the reverse sign of the errors shows that this is the best simultaneous description of the indirect and direct band gaps. The c parameter optimized for zb-AlN leads to a band gap underestimated of $\sim$9% for zb-GaN. One interesting property of the TB-mBJLDA potential is that the increase of the c parameter systematically reduces the difference between the indirect and direct band gaps of zb-AlN. For $c = 1$, we obtain a ratio of $E_{\mathrm{gap}}^{\text{zb-AlN}}(\Gamma_v \rightarrow X_c)/E_{\mathrm{gap}}^{\text{zb-AlN}}(\Gamma_v \rightarrow \Gamma_c) = 0.84$ for $c = 1.6$ this value increases to $E_{\mathrm{gap}}^{\text{zb-AlN}}(\Gamma_v \rightarrow X_c)/E_{\mathrm{gap}}^{\text{zb-AlN}}(\Gamma_v \rightarrow \Gamma_c) = 0.96$.

The calculated LDA-1/2 band gaps of $E_{\mathrm{gap}}^{\text{zb-AlN}}(\Gamma_v \rightarrow X_c) = 5.34$ eV, $E_{\mathrm{gap}}^{\text{zb-AlN}}(\Gamma_v \rightarrow \Gamma_c) = 5.87$ eV, and $E_{\mathrm{gap}}^{\text{zb-GaN}}(\Gamma_v \rightarrow \Gamma_c) = 3.31$ eV are an astonishing result. The relative error is significantly below 1% for all band gaps. Therefore also the ratio between the direct and the indirect band gap of zb-AlN is accurately reproduced. This feature singles out the LDA-1/2 approach from all other numerical approaches applied in this study, especially since these at least need separately adjusted parameters for both binary materials to reach the same accuracy. As stated above, these results were obtained by adding self-energy correction potentials to the N$_{2p}$
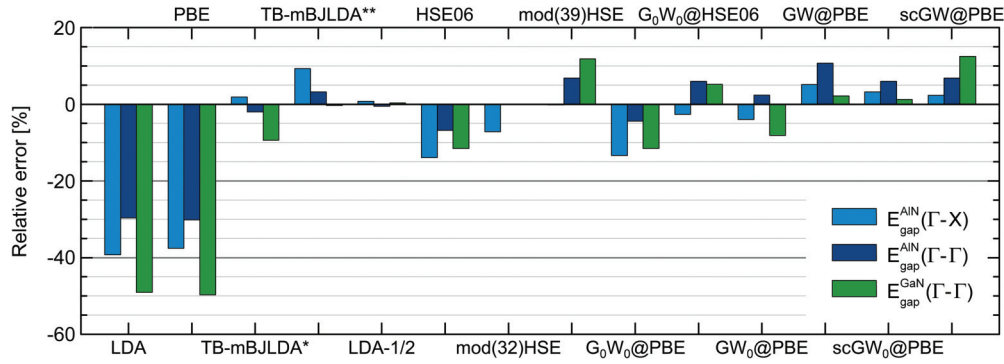
FIG. 5. (Color online) Relative percentaged errors $(E_{gap}^{calc} - E_{gap}^{exp})/E_{gap}^{exp} \, 100$ of the calculated direct $\Gamma_v \to \Gamma_c$ and indirect $\Gamma_v \to X_c$ band gaps of zb-AlN and the direct zb-GaN band gap. TB-mBJLDA* and TB-mBJLDA** refer to c parameters of $c = 1.45$ and 1.55. For HSE-type calculations, the used fraction of exact exchange is indicated in brackets. In partially and fully self-consistent GW calculations, the QP eigenvalues have been updated eight times to reach self-consistency. In the scGW_0 and scGW schemes, also updates of the one-electron orbitals have been considered. The absolute band gap values corresponding to this diagrammatic representation are summarized in Table III.

states for zb-AlN and to the N_{2p} and Ga_{3d} states for zb-GaN. The LDA-1/2 band gaps are predominantly influenced by self-energy corrections to the N_{2p} states. Considering only the N_{2p} state self-energy corrections for calculations on zb-GaN results in a slightly smaller band gap of $E_{gap}^{zb\text{-}GaN}(\Gamma_v \to \Gamma_c) = 3.15$ eV. Additional Al_{2p} self-energy corrections increase the zb-AlN band gaps to $E_{gap}^{zb\text{-}AlN}(\Gamma_v \to X_c) = 5.42$ eV and $E_{gap}^{zb\text{-}AlN}(\Gamma_v \to \Gamma_c) = 6.05$ eV.

Next, we consider the band gap description in hybrid-functional DFT. Starting from the original HSE06 parameters, we find that a 25% exact SR exchange contribution, underestimates the band gaps between $\sim$7% and $\sim$14%. This is consistent with preceding studies that reported the best HSE performance for small and midgap semiconductors and a band gap underestimation for wide-gap semiconductors and insulators.[60,97,98] We systematically increased the exact exchange fraction α [cf. Eq. (8)] in our modified HSE-type hybrid functional calculations to determine the value for α best suited to reproduce the experimental data. 32% exact exchange [mod(32)HSE] exactly reproduces the direct band gaps of both bulk material. Simultaneously, the indirect zb-AlN band gap of $E_{gap}^{zb\text{-}AlN}(\Gamma_v \to X_c) = 4.92$ eV shows an $\sim$7% underestimation of the reported experimental value. The indirect band gap of zb-AlN is not reproduced until a Fock exchange fraction of $\sim$39% [mod(39)HSE] is used. The difference of the indirect and direct zb-AlN band gaps is close to 1 eV independently of the exact-exchange fraction thus above the 0.6 eV difference between the experimental values. Based on these observations it seems reasonable to introduce a composition-dependent exact exchange fraction in the HSE hybrid-functional description of the ternary zb-$Al_xGa_{1-x}N$ alloys.

Finally, we address the manifold of GWA based QP theory approaches starting with the non-self-consistent G_0W_0 results obtained in first order perturbation theory according to Eq. (12). G_0W_0 QP corrections, obtained from DFT-PBE one-electron orbitals (i.e., G_0W_0@PBE), increase the DFT band gaps to values very similar to the HSE06 results. A G_0W_0@PBE band gap underestimation between $\sim$4% and $\sim$13% is observed. Since the results of the non-self-consistent

GWA critically depend on the initial wavefunctions, one-electron orbitals from HSE hybrid-functional calculations are a significantly improved basis to evaluate the QP shifts. Consequently, the G_0W_0@HSE06 QP band gaps of $E_{gap}^{zb\text{-}AlN}(\Gamma_v \to X_c) = 5.16$ eV, $E_{gap}^{zb\text{-}AlN}(\Gamma_v \to \Gamma_c) = 6.25$ eV, and $E_{gap}^{zb\text{-}GaN}(\Gamma_v \to \Gamma_c) = 3.47$ eV are significantly closer to the fundamental experimental band gaps within an error range from $\sim$$-3$% to $\sim$6%. Thereby, the direct $\Gamma_v \to \Gamma_c$ band gaps are overestimated while the indirect zb-AlN band gap is still underestimated. With 1.09 eV the difference of indirect and direct zb-AlN band gap energies is close to the results of hybrid-functional DFT. Notably, the direct G_0W_0@HSE06 QP band gap exactly corresponds to the fundamental (direct) band gap of wz-AlN.[130] The results of the various self-consistent GW schemes are quite inconclusive with relative band gap errors between $\sim$$-8$% and $\sim$12%. No systematic trend in the QP band gaps is found. The partial inclusion of self-consistency in the scGW_0@PBE scheme is the only scheme that generates improved band gap data for the two materials considered in this study. The calculated band gaps of $E_{gap}^{zb\text{-}AlN}(\Gamma_v \to X_c) = 5.47$ eV, $E_{gap}^{zb\text{-}AlN}(\Gamma_v \to \Gamma_c) = 6.25$ eV, and $E_{gap}^{zb\text{-}GaN}(\Gamma_v \to \Gamma_c) = 3.34$ eV overestimate the experimental gaps by $\sim$1% to $\sim$6%. Another important observation is the relative close agreement ($<$ 0.13 eV) between the mod(39)HSE result and the QP band gaps obtained by fully self-consistent scGW@PBE calculations. This accordance implies two things. On the one hand, HSE-type hybrid functionals can be adjusted to reach even the QP band gap accuracy of sophisticated GW schemes. On the other hand, the mod(39)HSE wave functions are expected to be very close to the true QP wave functions. Summarizing, the results from the self-consistent GW approaches, even the best results represent only marginal improvements over the G_0W_0@HSE06 results. Further improvements most likely require the inclusion of additional vertex corrections to include the electron-hole interaction, that is neglected in all GWA schemes, into the self-consistency cycle.[75,84,112] Considering the lower computational cost, non-self-consistent G_0W_0 corrections obtained from high-quality (hybrid-functional DFT) one-electron orbitals, that follow the

originally intended idea of a perturbative approach, probably still represent a very meaningful approach to obtain reliable QP energies.

E. Band structure of zb-AlN and zb-GaN

In order to compare the electronic structure beyond the fundamental direct and indirect band gap transitions, we have visualized the TB-mBJLDA, LDA-1/2, modHSE, and G_0W_0@HSE06 band structures in Fig. 6. For the TB-mBJLDA and modHSE band structures the fundamental band gap optimized c parameters and exact exchange fractions were used. The G_0W_0@HSE06 QP band structure (see gray dots) is taken as reference for QP energies. Ignoring the strongly bound energy states that originate from the Ga_{3d} semicore and N_{2s} states for a moment, our modified HSE-type hybrid-functional calculations show an excellent agreement with the G_0W_0@HSE06 band structures for valence and conduction band states in both materials. This result again justifies the adjustment of the exact-exchange fraction in HSE-type hybrid-functional calculations to reproduce the GW QP band structure. As already indicted by the fundamental band gaps, the TB-mBJLDA and LDA-1/2 approaches both provide reasonable approximations to the QP band structure. Differences between TB-mBJLDA as well as LDA-1/2 energy bands and the G_0W_0@HSE06 band structures increase significantly with the excitation energy as well as the reciprocal lattice vector. This affects band-structure characteristics such as the effective masses. These deviations also affect the size and relative differences of energy transitions, as indicated by the lowest valence-to-conduction band transitions at the Γ, X, and L points sketched in Fig. 6. Differences are in particular obvious with respect to the modHSE band structures.

Compared to the G_0W_0@HSE06 QP energies, dramatic deviations are found for the low lying, stronger localized energy states. The N_{2s} valence-band states in zb-AlN are located between -13.3 and -16.1 eV in G_0W_0@HSE06. TB-mBJLDA surprisingly well reproduces the QP N_{2s} band with maximal differences of $\sim$0.7 eV (at the Γ point). Comparing the band energies at the Γ point, the LDA-1/2 calculation overestimates the position of the N_{2s} band energy by $\sim$1.7 eV. Equivalently, the mod(39)HSE band structure shows an N_{2s} band underestimation of $\sim$1.1 eV. From G_0W_0@HSE06 calculations the position of the Ga_{3d} bands in zb-GaN is found between $\sim$$-17$ and $\sim$$-18$ eV. The N_{2s} band is located at $\sim$$-18$ eV at the Γ point and thus partially hybridized with the Ga_{3d} states around the Γ point. The N_{2s} states at -13.7 eV are well separated from the Ga_{3d} states around the W point. In general, the character of the s-d coupling of N_{2s} and Ga_{3d} semicore states depends critical on the energy differences between both states. Ding *et al.*[131] used angle-resolved photoelectron spectroscopy to study the valence band structure of zb-GaN. In the high binding-energy region, a sharp peak at 17.7 eV has been assigned to the Ga_{3d} states, while a second less intense peak at 14.2 eV binding energy belongs to the N_{2s} states. The photoemission data further indicate a very clear separation of Ga_{3d} and N_{2s} states by 3.5 eV and a N_{2s} band width of 0.65 eV. Considering these experimental findings, our G_0W_0@HSE06 QP energies are in good agreement with the experiment except for the hybridization around the Γ point that

might be an artifact from the initial HSE06 hybrid-functional DFT wave functions.

The mod(39)HSE calculations approximately place the Ga_{3d} semicore and N_{2s} energy states in the same energy region (-13.3 to -17.8 eV) as obtained from G_0W_0@HSE06. In LDA-1/2, the occupied Ga_{3d} and N_{2s} states show the same qualitative result, but shifted to higher energies. Even the TB-mBJLDA energy bands show roughly the same band characteristics. All these calculations are affected by a hybridization of the electronic states that is even stronger than the hybridization found in the G_0W_0@HSE06 data. Generally, in all our calculations the Ga_{3d} and N_{2s} states occupy the same energy region. Compared to the undisturbed N_{2s} band in zb-AlN, the Ga_{3d} semicore states in a certain sense *cut* the s band of N into two branches that hybridize with the d sates. Thus one band with partial N_{2s} character is found below and one above the d-like energy bands. To single out the effects from using different numerical approaches, we should predominantly compare the position of the *inert* Ga_{3d} energy bands that are not notably affected by hybridization and that show the expected low-energy dispersion of a localized d band. The XC functional effect on the N_{2s} states could be estimated from the energy states at the W point. The mod(39)HSE QP calculation places the (inert) d bands at ~-16.0 eV, almost 2 eV above the G_0W_0@HSE06 d bands. For the N_{2s} states at -13.3 eV, the upward shift with respect to the G_0W_0@HSE06 position is about 0.5 eV. In LDA-1/2, the Ga_{3d} semicore states are shifted by > 4 eV to ~-13.7 eV and the anion N_{2s} states by ~ 2 eV to -11.3 eV. The TB-mBJLDA calculation finds the N_{2s} states at the same energy as in LDA-1/2. The Ga_{3d} states experience an additional shift of $\sim$1 eV to ~-12.6 eV.

Summarizing, our band structure calculations clearly demonstrate that calculations based on the TB-mBJLDA potential with a properly adjusted c parameter as well as the self-energy corrected LDA-1/2 approach allow the approximate description of QP band gap energies. The overall band topologies are in reasonable qualitative agreement close to the band edges. However, the relative differences in the transition energies at high-symmetry points might be critical for the description of the direct-indirect band gap crossover. Furthermore, important band-structure characteristics as the effective masses might deviate significantly from the QP result, as reported by other authors.[73] The position of the strongly localized low lying energy states are severely affected by an artificial hybridization in all applied approaches that is not seen in the experiment. Even the G_0W_0@HSE06 QP bands are still hybridized around the Γ point. HSE-type calculations reproduce the entire G_0W_0@HSE06 QP band structure over a wide-energy range with high accuracy. Table IV summarizes the lowest band-to-band transition energies of zb-AlN and zb-GaN at the Γ, X, and L points that are relevant for the interpretation of experimental data in the following section.

IV. BAND GAPS, TRANSITION ENERGIES, AND DIRECT-INDIRECT CROSSOVER

In order to discuss the band gaps of zb-$Al_xGa_{1-x}N$ we have to be able to identify and label the electronic states of the alloy consistently, which is not per se a trivial task. To begin
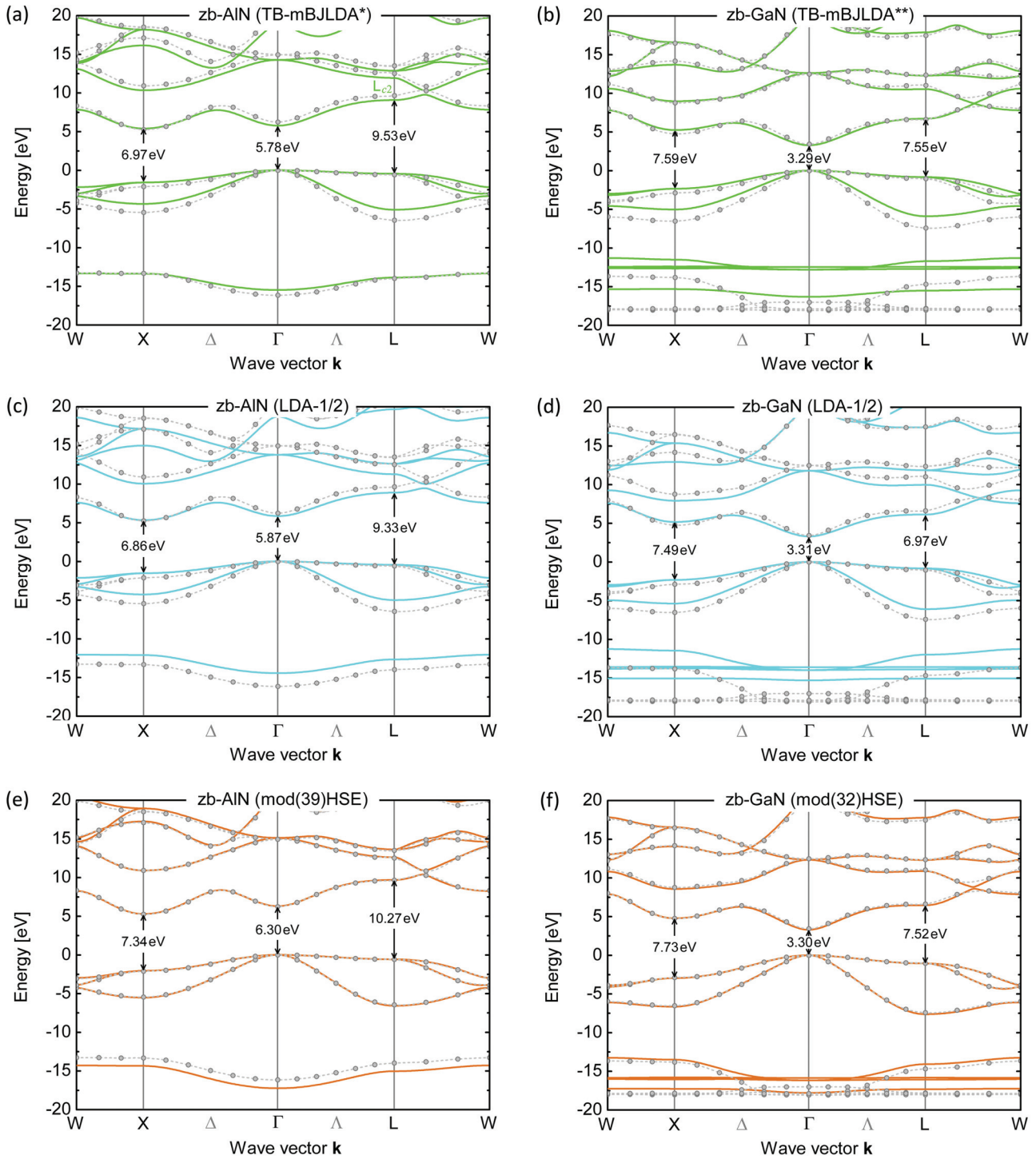
FIG. 6. (Color online) Band structure of zb-AlN and zb-GaN calculated by the TB-MBJLDA meta-GGA potential, the LDA-1/2 technique, and HSE-type hybrid functionals. TB-mBJLDA* and TB-mBJLDA** refer to optimized c parameters of $c = 1.45$ and 1.55. For HSE-type calculations, the used fraction of exact exchange is indicated in brackets. The direct band gaps at the Γ, L, and X points are indicated. The gray dots represent G_0W_0@HSE06 QP energies. The gray dashed lines are guidelines to the eyes.

with, the electronic states of the bulk materials are completely characterized by a band index, labeling the corresponding valence as well as conduction band, and a k-point index, labeling the position of the electronic state in the irreducible part of the Brillouin zone. Additionally, we have information about the symmetry of the corresponding one-electron orbitals

and thus the degeneracy of the corresponding eigenvalues. Type (direct/indirect) and size of the fundamental band gap are commonly determined by band structure calculations on a primitive unit cell of the periodic crystal lattice. Generally, the use of nonprimitive unit cells in the numerical description of the binary bulk materials gives rise to zone folding effects

TABLE IV. Summary of the two lowest valence-to-conduction band transitions at the Γ, X, and L high-symmetry points corresponding to the band gap data visualized in Fig. 6. Also the indirect $\Gamma_v \to X_c$ and $\Gamma_v \to L_c$ band gaps are included. TB-mBJLDA* and TB-mBJLDA** refer to optimized c parameters of $c = 1.45$ and 1.55. For HSE-type calculations the fraction of exact exchange is indicated in brackets. All transition energies are given in eV.

Band transition	TB-mBJLDA*	TB-mBJLDA**	LDA-1/2		mod(39)HSE	mod(32)HSE	G_0W_0@HSE06	
	zb-AlN	zb-GaN	zb-AlN	zb-GaN	zb-AlN	zb-GaN	zb-AlN	zb-GaN
$\Gamma_v \to \Gamma_c$	5.78	3.29	5.87	3.31	6.30	3.30	6.25	3.47
$\Gamma_v \to \Gamma_{c2}$	14.27	12.62	13.80	11.78	15.12	12.34	14.95	12.49
$X_v \to X_c$	6.97	7.59	6.86	7.49	7.34	7.73	7.36	7.65
$X_v \to X_{c2}$	11.92	11.31	11.58	10.24	12.97	11.52	13.04	11.65
$L_v \to L_c$	9.53	7.55	9.33	6.97	10.27	7.52	10.21	7.65
$L_v \to L_{c2}$	12.36	11.36	11.72	10.81	13.19	11.94	13.08	12.05
$\Gamma_v \to X_c$	5.40	5.25	5.34	5.17	5.29	4.78	5.16	4.77
$\Gamma_v \to L_c$	9.08	6.72	8.90	6.13	9.70	6.47	9.64	6.61

that map one or more irreducible k points onto k points in the new Brillouin zone. For instance, the threefold degenerate X_c states of zb-AlN in the primitive zinc-blende Brillouin zone are mapped onto the Γ point in a cubic unit-cell representation, but this is a pure zone-folding effect, the optical dipole-matrix elements remain unchanged and there is no influence on the fundamental direct/indirect nature of the electronic band gap. In contrast, the substitutional disorder, and to a very small extend the topological disorder due to local atomic relaxations, in a multicomponent semiconductor alloy lift the strict long-range order of the bulk material. Thus the Bloch theorem is not strictly valid, k is *not* a *good* quantum number anymore and the band gaps of the semiconductor alloy will, strictly speaking, become always direct. However, in contrast to a truly amorphous material, the one-electron orbitals in the substitutionally disordered crystal will remain similar to the states in the bulk material even close to the band edges. Therefore the nature of the alloy band gap will be different if the electronic states at the band edges are similar to electronic states forming a direct or an indirect bulk band gap. For zb-Al$_x$Ga$_{1-x}$N alloys in the Al-rich concentration range, the conduction band edge (at the Γ point) is formed by electronic states similar to the X_c states of zb-AlN. This band gap is only *pseudodirect*, since the dipole-matrix elements of such a band gap will always be similar to the indirect bulk transitions and thus smaller than those of a truly direct transition. It is common to reduce the terminology to describe the alloy completely to that of the bulk semiconductors, as already done in the introductory section. In the ternary zb-Al$_x$Ga$_{1-x}$N alloys, the electronic states, responsible for the band gaps in the pure bulk phases, intermix with respect to the relative Ga : Al concentration. It is possible to trace the bulklike electronic states throughout the whole composition range of the ternary alloy. In general, the critical point of the cation concentration that marks the transition of the fundamental alloy band gap from involving either the bulklike Γ_c conduction band states originating from zb-GaN or the bulklike X_c conduction band states of zb-AlN is called a direct-indirect band gap crossing/crossover instead of the more precise term *direct-to-pseudodirect* transition. The influence of alloy disorder is ultimately reflected in a lifted degeneracy of electronic states that are degenerate in zb-AlN

and zb-GaN. In a unit-cell approach, the degree of disorder and thus the degeneracy of the electronic states is directly related to a particular lattice configuration (i.e., local atomic structure) in a specific unit cell. To minimize the artificial *periodicity errors*, we take the average of the originally degenerate bulk-energy levels to extract the alloy band gaps.

In Fig. 7, the calculated zb-Al$_x$Ga$_{1-x}$N band gaps for eight atom unit cells (i.e., RAND 8) are plotted for various numerical approaches. The visualized band gap data especially confirm the relative close agreement between band gaps from non-self-consistent GW and HSE-type hybrid-functional DFT calculations over the entire composition range of zb-Al$_x$Ga$_{1-x}$N. In detail, the band gaps obtained from the unmodified HSE06 hybrid functional agree very well with G_0W_0@PBE QP band gaps. G_0W_0@HSE06 QP gaps are found to be in excellent agreement with the band gaps obtained from our modified HSE-type calculations. In the modHSE approach, the exact-exchange fraction α in the alloy is linearly
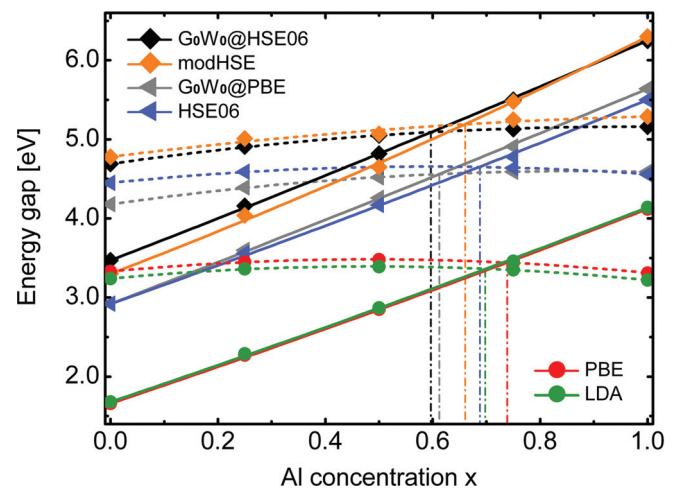

FIG. 7. (Color online) Fundamental alloy band gaps of zb-Al$_x$Ga$_{1-x}$N for cubic eigth atom unit cells (RAND 8). Symbols represent calculated values. Solid and dotted lines represent nonlinear fits according to Eq. (1) for the direct $\Gamma_v \to \Gamma_c$ type and indirect $\Gamma_v \to X_c$ type alloy band gaps. In modHSE calculations, the exact exchange fraction was linearly interpolated between $\alpha_{\text{AlN}} = 0.39$ and $\alpha_{\text{GaN}} = 0.32$.

TABLE V. Bowing parameters (in eV) of the direct $\Gamma_v \to \Gamma_c$ type and indirect $\Gamma_v \to X_c$ type zb-Al$_x$Ga$_{1-x}$N alloy band gaps [calculated via Eq. (1)] as well as critical Al concentration at the direct-indirect band gap crossover point.

Simulation method		Bowing parameter (eV)		Crossing
Method	Unit cell	b_Γ	b_X	x
PBE	RAND 8	0.17	−0.65	0.74
	RAND 64	0.50	−0.06	0.72
	RAND 216	0.56	−0.02	0.72
	SQS 8	0.15	−0.65	0.74
	SQS 16	0.50	−0.06	0.72
	SQS 32	0.55	−0.03	0.72
TB-mBJLDA	RAND 8	0.69	−0.21	0.88
	RAND 64	1.12	0.29	0.87
	RAND 216	1.17	0.30	0.88
LDA-1/2	RAND 8	0.60	−0.30	0.83
	RAND 64	0.86	0.08	0.82
	RAND 216	0.93	0.07	0.83
HSE06	RAND 8	0.22	−0.58	0.69
	RAND 64	0.53	−0.01	0.67
	RAND 216	0.59	0.01	0.69
	SQS 8	0.30	−0.35	0.68
	SQS 16	0.47	−0.08	0.67
	SQS 32	0.59	0.02	0.69
mod(32)HSE	RAND 8	0.21	−0.55	0.67
	RAND 64	0.54	0.00	0.65
	RAND 216	0.60	0.04	0.65
modHSE	RAND 8	0.40	−0.33	0.66
	RAND 64	0.53	0.05	0.64
	RAND 216	0.59	0.09	0.64
G_0W_0@PBE	RAND 8	0.11	−0.55	0.61
G_0W_0@HSE06	RAND 8	0.16	−0.50	0.60
G_0W_0@HSE06	SQS 8	0.11	−0.64	0.61
exp		0.85	0.01	0.71

interpolated between the optimized values of $\alpha_{\mathrm{AlN}} = 0.39$ for zb-AlN and $\alpha_{\mathrm{GaN}} = 0.32$ for zb-GaN. Thus a properly adjusted HSE-type functional allows us to calculate accurate QP band gaps even for the large unit-cell alloys that are computationally beyond the scope of even non-self-consistent GW calculations.

Subsequently, we discuss the Al-dependent bowing characteristics of the energy transitions in zb-Al$_x$Ga$_{1-x}$N alloys according to Eq. (1). All calculated bowing parameters, as well as the direct-indirect transition points are summarized in Table V. From the experimental transition energies (cf. Fig. 2), a bowing parameter of $b_\Gamma = 0.85$ eV for the direct $\Gamma_v \to \Gamma_c$ type band gap is obtained. In addition, no significant bowing is indicated in the $X_v \to X_c$ transition energies. In anticipation of the alignment of the E_2 transition energies discussed below, the indirect $\Gamma_v \to X_c$ type alloy band gap will preserve this characteristic, almost linear, dependence on the alloy composition.

Independent of the numerical methodology, the alloy band gaps of all eight atom unit-cell calculations visualized in Fig. 7 share common bowing characteristics. The direct $\Gamma_v \to \Gamma_c$ type band gaps in the zb-Al$_x$Ga$_{1-x}$N alloys show an increase with Al content that only weakly differs from a linear dependence as indicated by bowing parameters b_Γ between 0.11 and 0.22 eV, which significantly underestimate the experimental value. Only in the modHSE calculations a

notable downward bowing of 0.40 eV is indicated. The indirect $\Gamma_v \to X_c$ type band gap is characterized by a notable upward bowing with a b_X parameter between −0.50 and −0.65 eV, which is in disagreement with the linear dependence observed in the experimental data. Again a slightly improved value of $b_X = -0.33$ eV is obtained by modHSE calculations. As we will see in a moment, these bowing parameters are affected by the poor alloy description through cubic eight atom unit cells that are affected by spurious symmetry. The nonlinear curve fits in Fig. 7 further illustrate that an increased exact exchange fraction, changes the distinct downward bending at higher Al content in LDA/GGA DFT to a more constant progression in hybrid-functional DFT and G_0W_0 calculations. This directly influences the direct-indirect band gap transition that occurs in the high Al concentration range. In LDA and PBE DFT the transition concentration is $x = 0.70$ and 0.74, respectively. In HSE hybrid-functional DFT the critical Al content is found to decrease for a higher exact exchange fraction from $x = 0.69$ in conventional HSE06 to $x = 0.66$ in modHSE. The G_0W_0 QP results provide an even lower transition concentration of ~ 0.6. From the bowing parameters listed in Table V it is further obvious that both the TB-mBJLDA functional and the LDA-1/2 technique lead to significantly larger (more positive, less negative) bowing parameters that are closer to the experimental observations. Aside from the
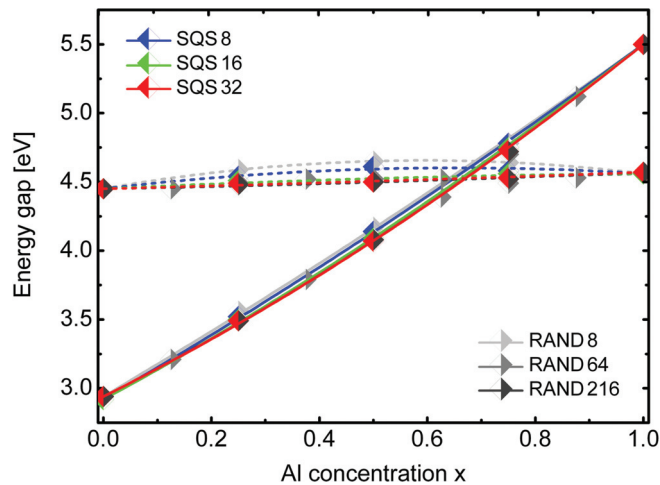
FIG. 8. (Color online) Calculated DFT-HSE06 alloy band gaps of zb-Al$_x$Ga$_{1-x}$N for various SQS and randomly occupied cubic unit-cell structure models (RAND). The symbols represent calculated values. Solid and dotted lines represent trend lines of the direct $\Gamma_v \rightarrow \Gamma_c$ type and indirect $\Gamma_v \rightarrow X_c$ type band gaps.

modHSE results, the bowing parameters increase by roughly 0.4 eV in TB-mBJLDA as well as LDA-1/2. As argued below, this assumed improvement rather represents a fortuitous than a systematic improvement by partially canceling the small unit-cell-induced periodicity errors with an overestimation of the bowing parameters.

In order to identify the artificial periodicity errors introduced by the small unit-cell representation of the zb-Al$_x$Ga$_{1-x}$N alloys, the HSE06 band gaps for all different structure models are displayed in Fig. 8. It is obvious that the Al-content dependent bowing characteristics of the alloy band gaps are significantly influenced by the unit-cell representation. Especially the indirect alloy band gap, obtained from the X_c-type energy states, is affected by such unit-cell periodicity errors. At $x = 0.5$, the difference between eight atom unit-cell calculations and calculations on the RAND 216 and SQS 32 alloy unit cells is largest (~ 0.15 eV). This behavior directly reflects the artificial alloy symmetry, which is necessarily largest for a 50:50 cation ratio due to the formation of a superlattice-type zb-AlN/GaN alloy. The periodicity error is slightly reduced by the SQS 8 structure that can be characterized as a staggered superlattice-type alloy [see Fig. 4(b)]. The SQS 16 alloy band gaps show just marginal deviations from the RAND 216 and SQS 32 alloy unit-cell results. The RAND 216, and SQS 32 unit-cell representations of the zb-Al$_x$Ga$_{1-x}$N alloy basically show identical band gap energies and fitting-curve characteristics. For both structure models, a notable bowing of the direct $\Gamma_v \rightarrow \Gamma_c$ type alloy band gap of $b_\Gamma = 0.59$ eV is obtained. The direct $\Gamma_v \rightarrow X_c$ type band gap shows a nearly linear increase over the complete composition range. This linear dependence nicely matches the linear dependence indicated in the experimental data. For both alloy representations (RAND and SQS), the direct-indirect band gap crossover is found at $x = 0.69$. The RAND 64 unit-cell calculations show band gap deviations $\leqslant 0.02$ eV from the RAND 216 and SQS 32 results and the nonlinear fitted band gap curves are almost identical to the results of

RAND 216 and SQS 32 unit cells. Also the Al content at the direct-indirect band gap crossover of $x = 0.67$ is only marginally affected.

In summary, the unit-cell representation of the randomly occupied zb-Al$_x$Ga$_{1-x}$N alloy suffers from notable periodicity errors for very small (eight atom) unit cells. This observation affects both unit-cell modeling approaches, even if the SQS 8 representation slightly reduces the periodicity errors. Compared to the largest 216 atom unit cells, the 32 atom SQS unit cells allow band gap calculations with a significantly reduced number of atoms without any notable loss of accuracy. The modeling of the zb-Al$_x$Ga$_{1-x}$N alloy seems to benefit significantly from the similar lattice characteristics of zb-AlN and zb-GaN. The direct-indirect band gap crossover concentration seems to be quite insensitive to the specific unit-cell representation, since both the direct-type and the indirect-type alloy band gap are equally affected by the artificially introduced lattice periodicity. In fact, the differences in the direct-indirect band gap crossing point between eight atom unit cells and the 32 atom SQSs as well as the RAND 216 unit cells never exceeds 0.02 (cf. Table V) for the various numerical approaches. Thus even the critical Al concentrations for the direct-indirect crossing from eight atom unit cells are very reasonable.

While the direct-indirect band gap crossing is weakly affected by the unit-cell representation, the bowing parameters show a significant dependence on the alloy modeling. The unit-cell representation related trends in the bowing parameters, discussed above for the conventional HSE06 hybrid functional, are found to be qualitatively very similar in the other numerical approaches. The more accurate (i.e., less symmetric and *more random*) alloy representation always increases the downward bowing b_Γ of the direct $\Gamma_v \rightarrow \Gamma_c$ type alloy band gap. The smallest increase (0.19 eV) is found in the modHSE approach. However, modHSE already predicted a notable bowing for eight atom unit cells. For the other XC functionals b_Γ increases between 0.29 eV (HSE06, SQS unit cells) and 0.48 eV (TB-mBJLDA, RAND unit cells). For LDA-1/2 and TB-mBJLDA, the increase of the bowing parameter even results in an overestimation of the experimental bowing parameter of $b_\Gamma = 0.85$ eV by 0.08 eV in LDA-1/2 and 0.32 eV in TB-mBJLDA. Alongside the observed increase of the $\Gamma_v \rightarrow \Gamma_c$ type gap for all XC functionals, the indirect $\Gamma_v \rightarrow X_c$ type alloy band gap shows an even stronger increase (between 0.37 eV in HSE06 and 0.63 eV in PBE) of the bowing parameter b_X. While the results of eight atom unit-cell calculations indicate a notable upward bowing by negative values of b_X for all numerical approaches, the larger alloy unit cells reproduce the expected linear dependence on x very well. With exception of $b_X = 0.30$ eV in TB-mBJLDA, all numerical approaches yield bowing parameters b_X between -0.03 eV (PBE, RAND unit cells) and 0.09 eV (modHSE, RAND unit cells).

Surprisingly, the comparison of bowing parameters and direct-indirect crossing points shows that, despite the severe band gap underestimation, the results of calculations using the conventional semilocal PBE functional are very close to the HSE-type hybrid functional data. This indicates that the fundamental direct and indirect zb-Al$_x$Ga$_{1-x}$N alloy band gaps are rigidly narrowed in the DFT-PBE approach over the entire composition range. In contrast, the LDA-1/2 and
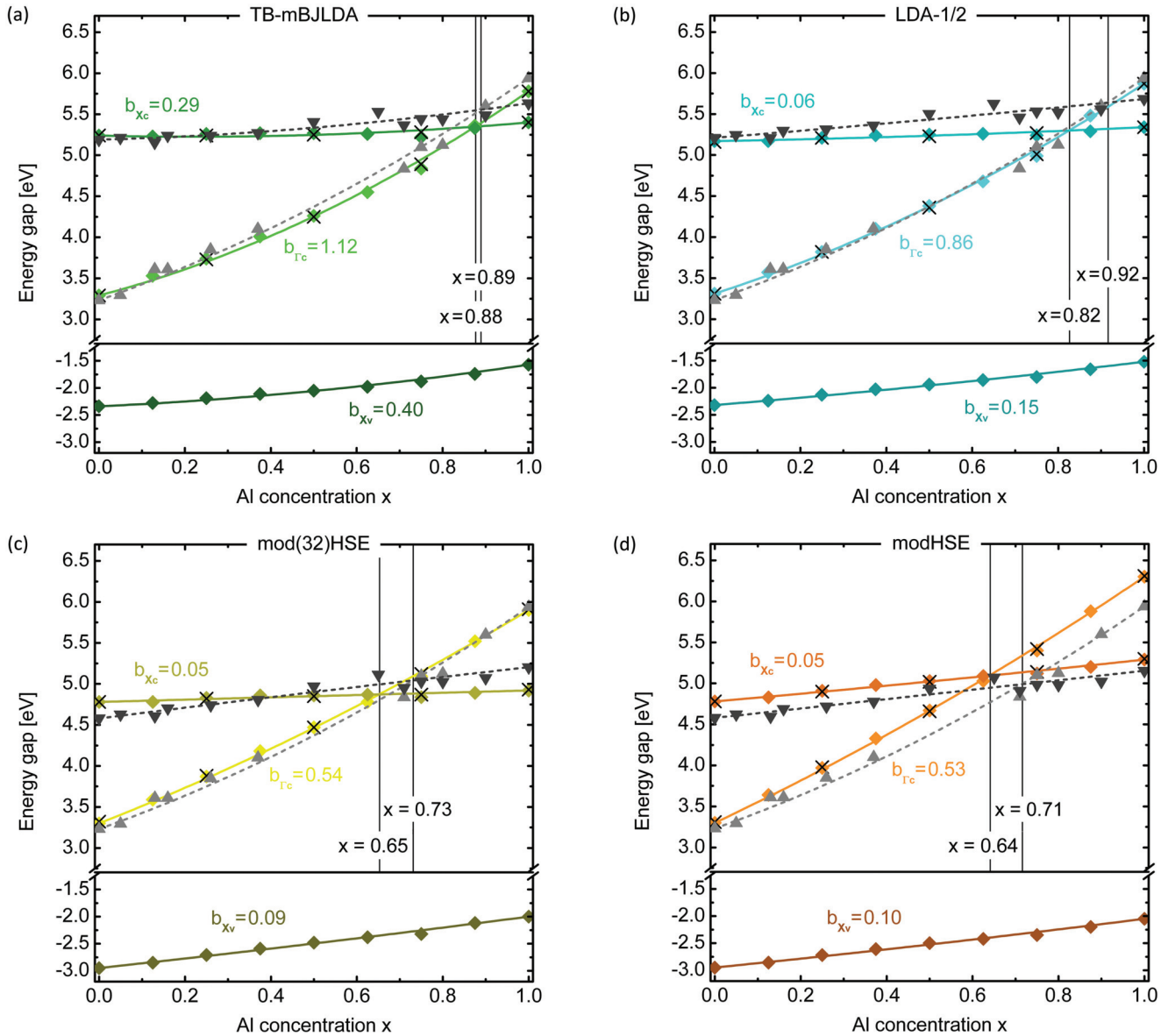
FIG. 9. (Color online) Fundamental alloy band gaps (upper panels) and position of the highest X point valence state (lower panel) of zb-Al$_x$Ga$_{1-x}$N calculated using (a) the TB-mBJLDA (c parameter linear interpolated between $c_{AlN} = 1.45$ and $c_{GaN} = 1.55$), (b) LDA-1/2 (self-energy corrections to N$_{2p}$ and Ga$_{3d}$ states), (c) mod(32)HSE (exact exchange fraction of $\alpha = 0.32$ for all Al concentrations), and (d) modHSE (exact exchange fraction linear interpolated between $\alpha_{AlN} = 0.39$ and $\alpha_{GaN} = 0.32$) approaches. Diamonds represent the calculated band gaps for randomly occupied 64 atom unit cells. Crosses indicate the corresponding band gaps from 216 atom unit cells. Solid and dotted lines represent nonlinear band gap fits according to Eq. (1). b_{Γ_c} and b_{X_c} are the bowing parameters of the direct $\Gamma_v \rightarrow \Gamma_c$ type and indirect $\Gamma_v \rightarrow X_c$ type alloy band gaps. b_{X_v} is the bowing parameter of the highest valence state at the X point. The position of the direct-indirect band gap crossover is indicated. Also included (light and dark gray symbols and lines) are the experimental transition energies (aligned according to the position of the X point valence states visualized in the lower panel) and nonlinear band gap fits.

TB-mBJLDA bowing parameters and the particular direct-indirect band gap crossing points show significantly larger deviations from the hybrid functional DFT results than the DFT-PBE results. Both LDA-1/2 and TB-mBJLDA predict very high Al concentrations ($x = 0.83$ in LDA-1/2 and $x = 0.88$ in TB-mBJLDA) at the direct-indirect band gap crossing. While LDA-1/2 calculations result in a slight overestimation of bowing parameters, TB-mBJLDA severely overestimates the bowing.

In Fig. 9, the $\Gamma_v \rightarrow \Gamma_c$ and $\Gamma_v \rightarrow X_c$ type alloy band gaps of zb-Al$_x$Ga$_{1-x}$N are plotted for the TB-mBJLDA

and LDA-1/2 methods as well as for two HSE-type hybrid functional approaches. Besides the modHSE approach, a HSE-type hybrid functional with an exact-exchange fraction of 32% [mod(32)HSE] was used over the entire alloy composition range. The mod(32)HSE approach allows the simultaneous exact reproduction of the direct experimental $\Gamma_v \rightarrow \Gamma_c$ band gaps of zb-AlN and zb-GaN (cf. Table III). The modHSE approach accurately reproduces the experimental values of the direct $\Gamma_v \rightarrow \Gamma_c$ band gap of zb-GaN and the indirect $\Gamma_v \rightarrow X_c$ band gap of zb-AlN. The TB-mBJLDA and LDA-1/2 techniques have already proven to allow the

approximate calculation of bulk-QP band gaps with high accuracy.

Figure 9 also contains the position and the corresponding bowing parameter b_{X_v} of the highest valence state at the X point (lower panels) over the entire composition range. For each numerical approach considered in Fig. 9, the X point valence states have been used to align the measured direct $X_v \rightarrow X_c$ type transition energies (cf. E_2 transition energies in Fig. 2) in order to extract the position of the *experimental* direct-indirect band gap crossing point.

(1) TB-mBJLDA: The direct-type zb-Al$_x$Ga$_{1-x}$N alloy band gaps from TB-mBJLDA calculations agree reasonably with the experiment, even if the calculated bowing parameter $b_\Gamma = 1.12$ eV significantly exceeds the experimental bowing of $b_\Gamma = 0.85$ eV. The indirect-type alloy band gap is characterized by a downward bowing of $b_X = 0.29$ eV. Compared to the other simulation approaches, the distinct bowing characteristics seem to be related to the TB-mBJLDA valence band structure. Also, the highest X point valence state of zb-Al$_x$Ga$_{1-x}$N shows a notable bowing of 0.4 eV throughout the alloy [cf. Fig. 9(a)] that is not reproduced in any other approach. Already in the TB-mBJLDA band structure calculations for the binary zinc-blende semiconductors [cf. Figs. 6(a) and 6(b)] a strong upward shift of the highest valence band around the X point with respect to the G_0W_0@HSE06 QP band structure was indicated. Hence the position of the indirect type alloy band gap seems to be overestimated over the entire composition range and the direct-indirect crossover point ($x = 0.89$) is shifted to far into the Al rich regime. The TB-mBJLDA alignment of the experimental transition energies leads to a very similar crossover point of $x = 0.88$. Although, the calculated TB-mBJLDA transition energies are fortuitously close to the experimental ones, the alignment by TB-mBJLDA valence states seems to be an improper choice for obtaining the accurate position of the direct-indirect band gap grossing point.

(2) LDA-1/2: LDA-1/2 reproduces the experimentally observed $\Gamma_v \rightarrow \Gamma_c$ type alloy band gaps very well. The calculated bowing of $b_\Gamma = 0.86$ eV almost perfectly reproduces the experimental bowing. The bowing parameter $b_X = 0.06$ eV indicates an almost linear dependence of the indirect $\Gamma_v \rightarrow X_c$ type alloy band gap on the Al content in LDA-1/2 calculations. Similar to TB-mBJLDA, the direct-indirect band gap crossover Al concentration is found at $x = 0.82$ well in the Al rich regime. The LDA-1/2 alignment of the experimental transition energies shifts the crossover point to an even higher Al concentration of $x = 0.92$. Analog to TB-mBJLDA the high Al crossover concentration seems to be the consequence of artificially high lying X point type valence states, that is as well indicated in the LDA-1/2 band structure of the binary semiconductors [cf. Figs. 6(c) and 6(d)]. In fact, the energy differences between the highest X point type valence band states are $\leqslant 0.15$ eV between TB-mBJLDA and LDA-1/2 calculations. Obviously, the inaccurate reproduction of QP valence band features in TB-mBJLDA as well as LDA-1/2, especially the relative energy difference between the highest Γ and X point type valence states, seems to fudge the direct-indirect band gap crossing point. The limitations of TB-mBJLDA and LDA-1/2 are best illustrated by comparison to the HSE-type hybrid functional data.

(3) mod(32)HSE: The mod(32)HSE alloy band gaps are found to be a good approximation of the measured $\Gamma_v \rightarrow \Gamma_c$ type direct alloy band gaps. However, the calculated bowing parameter of $b_\Gamma = 0.54$ eV underestimates the experimental bowing parameter notably. The indirect $\Gamma_v \rightarrow X_c$ type band gaps of zb-Al$_x$Ga$_{1-x}$N show a close to linear dependence ($b_X = 0.05$ eV) on the Al concentration and the direct-indirect band gap crossing is found at an Al:Ga ratio of 1.54 ($x = 0.65$). This value is significantly smaller than the crossover concentrations in TB-mBJLDA and LDA-1/2. Compared to TB-mBJLDA and LDA-1/2 the X point energies, necessary for the transition energy alignment, are reduced by roughly 0.5 eV and the bowing of 0.09 eV indicates an almost linear dependence of the valence states on the alloy composition. Consequently, the mod(32)HSE alignment of the experimental transition energies predicts a lower direct-indirect band gap crossing point of $x = 0.73$ than obtained for the TB-mBJLDA and LDA-1/2 alignments. In addition, an almost linear trend in the indirect $\Gamma_v \rightarrow X_c$ type alloy band gap is indicated after the alignment. In the middle of the composition range, the indirect $\Gamma_v \rightarrow X_c$ band gaps from the mod(32)HSE approach and the aligned experimental transition energies agree very well. However, through a slight mod(32)HSE overestimation of the indirect type gap, in the Ga-rich composition range and an underestimation at Al-rich conditions, the slope of the indirect $\Gamma_v \rightarrow X_c$ type alloy band gap with Al content x differs. mod(32)HSE predicts a much weaker slope than the one actually found for the aligned experimental transition energies.

(4) modHSE: In modHSE the overall agreement between the pure theoretical description and the modHSE aligned experimental data is very reasonable with respect to the qualitative features, while an overall overestimation of the experimental data is obvious. Compared to mod(32)HSE, the indirect $\Gamma_v \rightarrow X_c$ type alloy band gap increases almost linear as well, as indicated by an identical bowing parameter of $b_X = 0.05$ eV. However, the slope in modHSE is much closer to the aligned experimental data. Similar to mod(32)HSE, the direct-indirect band gap crossing is found at $x = 0.64$ in the modHSE calculations and at $x = 0.71$ from the aligned experimental transition energies. The common features between both hybrid functional approaches are also related to the quite similar description of the valence band structure. The position of the highest X point valence states is almost identical in the mod(32)HSE and the mod HSE approaches. The largest differences occur at Al-rich conditions and shift the X point valence states in modHSE by $\leqslant -0.05$ eV with respect to the mod(32)HSE energies. Even if there is a systematic overestimation of all experimentally determined energy gaps, we expect the modHSE results to be a very accurate and the most reasonable approximation to the true QP band structure of zb-Al$_x$Ga$_{1-x}$N alloys. This statement is based on two observation. On the one hand, we know that the modHSE calculations reproduce all G0W0@HSE06 QP alloy gaps within deviations $\leqslant 0.2$ eV [cf. Fig. 7 for the alloys and Figs. 6(e) and 6(f) for the binary semiconductors]. On the other hand, the modHSE approach reproduces all experimentally observed features of the alloy band gap dependence on the Al concentration with an nearly constant offset <200 meV. This offset is explainable by the difference between calculated QP

band gaps and experimental band gaps obtained by optical measurements (→ optical gaps) at room temperature. As already discussed in the experimental section, temperature effects, mediated by the electron-phonon coupling, seem to be responsible for an downward shift of the absorption edge in zb-$Al_xGa_{1-x}N$ alloys of approximately 100 meV as indicated in Fig. 3 for zb-AlN. To a small extend, also, the neglected spin-orbit interaction might be responsible for the observed difference between the experimental and theoretical data. Finally, the general influence of excitonic contributions through electron-hole interaction has already been discussed above in Sec. II.

In summary, TB-mBJLDA and LDA-1/2 allow a rough estimation of bowing parameters and the band gap crossover point. Considering the electronic structure characteristics, both approaches certainly fall into the same accuracy class. In consideration of the very moderate computational cost, our results support the use of both approaches to approximate the QP band structure for large unit cells of alloys, surfaces, and other nanostructured systems. Choosing between the two approaches, LDA-1/2 seems to be a slightly more reliable choice for approximate QP calculations. However, apart from the compensation of the band gap underestimation, even conventional semilocal DFT approaches (here, the PBE XC functional) might outperform the TB-mBJLDA and LDA-1/2 approaches in predicting electronic structure parameters as the band gap crossover points in semiconductor alloys. If reliable QP properties are desired, hybrid-functional approaches seem to be the best choice to obtain QP band gaps, band structures, and further characteristics of the electronic structure, at least if an accurate treatment of self-energy corrections within MBPT is computationally off-limits. Using an Al-concentration dependent exact-exchange parameter in HSE hybrid-functional calculations, the direct $\Gamma_v \rightarrow \Gamma_c$ type and indirect $\Gamma_v \rightarrow X_c$ type zb-$Al_xGa_{1-x}N$ alloy band gaps are given by $E_{gap,\Gamma}^{zb-Al_xGa_{1-x}N}(x) = 6.30x + 3.30(1-x) - 0.53x(1-x)$ eV and $E_{gap,X}^{zb-Al_xGa_{1-x}N}(x) = 5.29x + 4.78(1-x) - 0.05x(1-x)$ eV, respectively.

In Fig. 10, the measured energy transitions of Fig. 2 are aligned according to the energy positions of the highest L_v and X_v valence states (relative to the Γ point valence band maximum) taken from modHSE calculations on 64 atom unit cells. As stated above, also the high-energy optical transitions show a nonlinear dependence on the Al concentration. The E_1 transition energies, originating from fundamental $L_v \rightarrow L_c$ transitions, are in good agreement with the modHSE data. However, the corresponding bowing parameters are inconsistent. The experimental data indicate an pronounced upward bowing of $b_L = -0.59$ eV while the hybrid-functional data show a strong downward bowing characterized by a bowing parameter of $b_L = 1.05$ eV. Also, for E_0' transitions from the Γ_v valence band edge to the second conduction band Γ_{c2}, a reasonable agreement of theoretical and experimental transition energies is found while the bowing parameters differ. Bowing parameters of $b_{E_0'} = 0.42$ eV and $b_{E_0'} = -0.10$ eV are obtained from analyzing the experimental and modHSE data, respectively. For the E_1' and E_2' transition energies, it is not possible to prove the assumed correspondence to the high-energy $L_v \rightarrow L_{c2}$ and $X_v \rightarrow X_{c2}$ type energy transitions
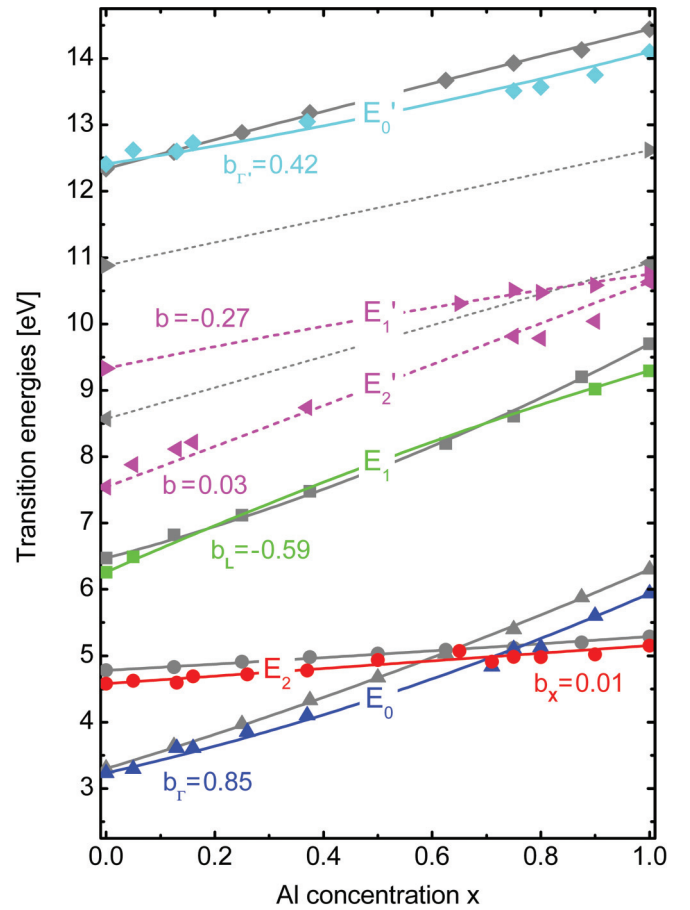

FIG. 10. (Color online) Analysis of Γ, L, and X point type fundamental (E_0, E_1, E_2) and high energy transitions (E_0', E_1', E_2') in zb-$Al_xGa_{1-x}N$ as a function of the Al content. Symbols indicate measured transition energies (cf. Fig. 2) aligned according to the energy positions of the highest L_v and X_v valence states (relative to the Γ point valence band maximum) taken from modHSE calculations on 64 atom unit cells. Lines represent nonlinear fits according to Eq. (1). Also included (gray symbols and lines) are the corresponding modHSE band gap energies and nonlinear curve fits.

(plotted in Fig. 10 as dotted gray lines form modHSE bulk data). This indicates that these optical transitions do not directly originate from transitions between high-symmetry point type electronic states.

We conclude our study by a comparison of our current experimental data to experimental data on zb-$Al_xGa_{1-x}N$ alloys reported in literature so far. While deviations of earlier cathodoluminescence measurements to the present data[24] are obvious from Fig. 11, the reflectivity measurement band gap data of Guerrero *et al.*[23] agree rather well with our measured alloy band gaps. However, a nonlinear band gap fit of the Guerrero *et al.* data gives a notable downward bowing of $b_\Gamma = 1.18$ eV larger than the bowing parameter of $b_\Gamma = 0.85$ eV from the present ellipsometry data. In consideration of the photoluminescence data of Nakadaira and Tanaka[26] that show a linear increase of the fundamental alloy band gaps in the Ga-rich composition region, we have additionally calculated separate nonlinear modHSE band gap fits for the direct alloy band gap below and above the direct-indirect band gap crossover. The band gap up to the band gap crossover
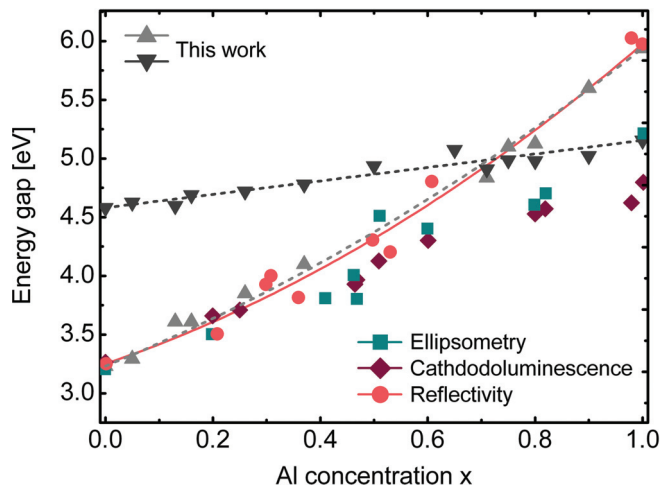
FIG. 11. (Color online) Experimental alloy band gaps of zb-$Al_x Ga_{1-x}$N. Black and gray triangles represent alloy band gaps determined from the ellipsometry data of this study. Solid and dotted lines represent nonlinear fits according to Eq. (1) for the direct $\Gamma_v \rightarrow \Gamma_c$ type and indirect $\Gamma_v \rightarrow X_c$ type band gaps. Reflectivity data (dots) are reproduced from Ref. 23 and cathodoluminescence (diamonds) and ellipsometry (squares) data from Ref. 24.

point is approximately linear, as indicated by a bowing of $b_\Gamma^{\text{Ga-rich}} = 0.06$ eV. In the Al-rich composition range above the direct-indirect crossover point, the separately calculated bowing parameter of $b_\Gamma^{\text{Al-rich}} = 0.11$ eV also indicates a weak downward bowing. Obviously, the nature of the direct zb-$Al_x Ga_{1-x}$N alloy bowing parameter appears significantly different, if only the Ga-rich or Al-rich regimes are considered.

V. SUMMARY

In this study, we have investigated the nature of the fundamental zb-$Al_x Ga_{1-x}$N alloy band gap. The existence and value of the critical direct-indirect band gap crossover as well as band gap bowing parameters have been determined by a series of calculations of various levels of sophistication and from the interpretation of critical points in the dielectric functions obtained from ellipsometry measurements. Our results show the interpretation of the measured data depends critically on the quality of the underlying electronic structure calculation.

The ellipsometry data indicate an downward bowing of the direct $\Gamma_v \rightarrow \Gamma_c$ type alloy band gap of $b_\Gamma = 0.85$ eV. The indirect $\Gamma_v \rightarrow X_c$ type band gap shows a linear dependence on

the Al concentration ($b_X = 0.01$ eV). The direct-indirect band gap crossover in zb-$Al_x Ga_{1-x}$N is found at $x = 0.71$ after aligning the experimentally obtained E_2 transition energies according to the highest X point valence-state energies in hybrid-functional DFT.

We have extensively tested the adaptability of the TB-mBJLDA and LDA-1/2 approaches to calculate approximate QP energies. Considering the computational cost which is comparable to (semi)local DFT calculations, both approaches allow an efficient description of QP band-structure characteristics. Both approaches give highly accurate bulk-band gaps for zb-AlN and zb-GaN. Nevertheless, they cannot compete with the HSE-type hybrid-functional description of the electronic structure of the zb-$Al_x Ga_{1-x}$N alloys. This is especially reflected in overestimated bowing parameters and a too high Al concentration at the direct-indirect band gap crossover. Also, the position of valence bands, crucial to align the experimentally determined transition energies in order to determine the direct-indirect band gap crossing, is severely affected by the use of the more *approximate* QP approaches TB-mBJLDA and LDA-1/2. Basically, the observed properties of the TB-mBJLDA functional and to a lesser extend the results obtained via the LDA-1/2 technique reflect the limited adaptability of a purely local XC functional. Even the semilocal PBE functional might give better bowing characteristics and a significantly more accurate estimation of the direct-indirect band gap crossover point. Hybrid functional DFT with an optimized exact exchange fraction reproduces QP alloy band gaps from $G_0 W_0$@HSE06 calculations within 0.2 eV over the entire alloy composition range. The calculated direct-indirect band gap crossover between $x = 0.64$ and 0.69 in hybrid functional DFT is found in good agreement with our experimental findings.

*Corresponding author: landmann@mail.upb.de

[1] V. Yu. Davydov, A. A. Klochikhin, R. P. Seisyan, V. V. Emtsev, S. V. Ivanov, F. Bechstedt, J. Furthmüller, H. Harima, A. V. Mudryi, J. Aderhold, O. Semchinova, and J. Graul, Phys. Status Solidi B **229**, R1 (2002).

[2] J. Li, K. B. Nam, M. L. Nakarmi, J. Y. Lin, H. X. Jiang, P. Carrier, and S.-H. Wei, Appl. Phys. Lett. **83**, 5163 (2003).

[3] E. Silveira, J. A. Freitas, Jr., M. Kneissl, D. W. Treat, N. M. Johnson, G. A. Slack, and L. J. Schowalter, Appl. Phys. Lett. **84**, 3501 (2004).

[4] P. Schley, R. Goldhahn, C. Napierala, G. Gobsch, J. Schörmann, D. J. As, K. Lischka, M. Feneberg, and K. Thonke, Semicond. Sci. Technol. **23**, 055001 (2008).

[5] M. P. Thompson, G. W. Auner, T. S. Zheleva, K. A. Jones, S. J. Simko, and J. N. Hilfiker, J. Appl. Phys. **89**, 3331 (2001).

[6] J. S. Im, H. Kollmer, J. Off, A. Sohmer, F. Scholz, and A. Hangleiter, Phys. Rev. B **57**, R9435 (1998).

[7] S.-H. Park and S.-L. Chuang, J. Appl. Phys. **87**, 353 (2000).

[8] F. Bernardini, V. Fiorentini, and D. Vanderbilt, Phys. Rev. B **56**, R10024 (1997).

[9]P. Waltereit, O. Brandt, A. Trampert, H. T. Grahn, J. Menninger, M. Ramsteiner, M. Reiche, and K. H. Ploog, Nature **406**, 865 (2000).

[10]G. Ramìrez-Flores, H. Navarro-Contreras, A. Lastras-Martìnez, R. C. Powell, and J. E. Greene, Phys. Rev. B **50**, 8433 (1994).

[11]B. Daudin, G. Feuillet, J. Hübner, Y. Samson, F. Widmann, A. Philippe, C. Bru-Chevallier, G. Guillot, E. Bustarret, G. Bentoumi, and A. Deneuville, J. Appl. Phys. **84**, 2295 (1998).

[12]J. Schörmann, S. Potthast, D. J. As, and K. Lischka, Appl. Phys. Lett. **89**, 131910 (2006).

[13]T. Schupp, K. Lischka, and D. J. As, J. Cryst. Growth **312**, 1500 (2010).

[14]S. V. Novikov, C. T. Foxon, and A. J. Kent, Phys. Status Solidi A **207**, 1277 (2010).

[15]E. A. DeCuir, Jr., E. Fred, M. O. Manasreh, J. Schörmann, D. J. As, and K. Lischka, Appl. Phys. Lett. **91**, 041911 (2007).

[16]D. J. As, Microelectron. J. **40**, 204 (2009).

[17]H. Machhadani, P. Kandaswamy, S. Sakr, A. Vardi, A. Wirtmüller, L. Nevou, F. Guillot, G. Pozzovivo, M. Tchernycheva, A. Lupu, L. Vivien, P. Crozat, E. Warde, C. Bougerol, S. Schacham, G. Strasser, G. Bahir, E. Monroy, and F. H. Julien, New J. Phys. **11**, 125023 (2009).

[18]E. Tschumak, R. Granzner, J. K. N. Lindner, F. Schwierz, K. Lischka, H. Nagasawa, M. Abe, and D. J. As, Appl. Phys. Lett. **96**, 253501 (2010).

[19]N. Zainal, S. V. Novikov, C. J. Mellor, C. T. Foxon, and A. J. Kent, Appl. Phys. Lett. **97**, 112102 (2010).

[20]C. Mietze, M. Landmann, E. Rauls, H. Machhadani, S. Sakr, M. Tchernycheva, F. H. Julien, W. G. Schmidt, K. Lischka, and D. J. As, Phys. Rev. B **83**, 195301 (2011).

[21]W. Yi, V. Narayanamurti, H. Lu, M. A. Scarpulla, A. C. Gossard, Y. Huang, J.-H. Ryou, and Russell D. Dupuis, Appl. Phys. Lett. **95**, 112102 (2009).

[22]M. Röppischer, R. Goldhahn, G. Rossbach, P. Schley, C. Cobet, N. Esser, T. Schupp, K. Lischka, and D. J. As, J. Appl. Phys. **106**, 076104 (2009).

[23]E. Martinez-Guerrero, F. Enjalbert, J. Barjon, E. Bellet-Almaric, B. Daudin, G. Ferro, D. Jalabert, L. S. Dang, H. Mariette, Y. Monteil, and G. Mula, Phys. Status Solidi A **188**, 695 (2001).

[24]H. Okumura, T. Koizumi, Y. Ishida, H. Yaguchi, and S. Yoshida, Phys. Status Solidi B **216**, 211 (1999).

[25]M. Feneberg, M. Röppischer, C. Cobet, N. Esser, J. Schörmann, T. Schupp, D. J. As, F. Hörich, J. Bläsing, A. Krost, and R. Goldhahn, Phys. Rev. B **85**, 155207 (2012).

[26]A. Nakadaira and H. Tanaka, Appl. Phys. Lett. **70**, 2720 (1997).

[27]B. Amin, I. Ahmad, M. Maqbool, S. Goumri-Said, and R. Ahmad, J. Appl. Phys. **109**, 023109 (2011).

[28]W. J. Fan, M. F. Li, T. C. Chong, and J. B. Xia, J. Appl. Phys. **79**, 188 (1996).

[29]W. J. Fan, M. F. Li, T. C. Chong, and J. B. Xia, Solid State Commun. **97**, 381 (1996).

[30]E. A. Albanesi, W. R. L. Lambrecht, and B. Segall, Phys. Rev. B **48**, 17841 (1993).

[31]J. W. D. Connolly and A. R. Williams, Phys. Rev. B **27**, 5169 (1983).

[32]S.-H. Wei, L. G. Ferreira, and A. Zunger, Phys. Rev. B **41**, 8240 (1990).

[33]S.-H. Wei, L. G. Ferreira, J. E. Bernard, and A. Zunger, Phys. Rev. B **42**, 9622 (1990).

[34]F. Sökeland, M. Rohlfing, P. Krüger, and J. Pollmann, Phys. Rev. B **68**, 075203 (2003).

[35]M. B. Kanoun, S. Goumri-Said, A. E. Merad, and H. Mariette, J. Appl. Phys. **98**, 063710 (2005).

[36]B.-T. Liou, Appl. Phys. A **86**, 539 (2007).

[37]A. Seidl, A. Görling, P. Vogl, J. A. Majewski, and M. Levy, Phys. Rev. B **53**, 3764 (1996).

[38]F. Fuchs, J. Furthmüller, F. Bechstedt, M. Shishkin, and G. Kresse, Phys. Rev. B **76**, 115109 (2007).

[39]C. B. Geller, W. Wolf, S. Picozzi, A. Continenza, R. Asahi, W. Mannstadt, A. J. Freeman, and E. Wimmer, Appl. Phys. Lett. **79**, 368 (2001).

[40]A. Zunger, S.-H. Wei, L. G. Ferreira, and J. E. Bernard, Phys. Rev. Lett. **65**, 353 (1990).

[41]B. Lee and L.-W. Wang, Phys. Rev. B **73**, 153309 (2006).

[42]D. Mourad and G. Czycholl, Eur. Phys. J. B **85**, 153 (2012).

[43]P. Soven, Phys. Rev. **156**, 809 (1967).

[44]B. Velický, S. Kirkpatrick, and H. Ehrenreich, Phys. Rev. **175**, 747 (1968).

[45]A. V. Ruban and I. A. Abrikosov, Rep. Prog. Phys. **71**, 046501 (2008).

[46]D. J. As and K. Lischka, in *Molecular Beam Epitaxy: From Quantum Wells to Quantum Dots; From Research to Mass Production*, edited by M. Henini (Elsevier, Amsterdam, 2013), Chap. 11, p. 203.

[47]C. Cobet, R. Goldhahn, W. Richter, and N. Esser, Phys. Status Solidi B **246**, 1440 (2009).

[48]C. Buchheim, R. Goldhahn, M. Rakel, C. Cobet, N. Esser, U. Rossow, D. Fuhrmann, and A. Hangleiter, Phys. Status Solidi B **242**, 2610 (2005).

[49]A. Riefer, F. Fuchs, C. Rödl, A. Schleife, F. Bechstedt, and R. Goldhahn, Phys. Rev. B **84**, 075218 (2011).

[50]W. Kohn and L. J. Sham, Phys. Rev. **140**, A1133 (1965).

[51]P. Hohenberg and W. Kohn, Phys. Rev. **136**, B864 (1964).

[52]J. P. Perdew and M. Levy, Phys. Rev. Lett. **51**, 1884 (1983).

[53]D. M. Ceperley and B. J. Alder, Phys. Rev. Lett. **45**, 566 (1980).

[54]J. P. Perdew and A. Zunger, Phys. Rev. B **23**, 5048 (1981).

[55]J. P. Perdew and Y. Wang, Phys. Rev. B **45**, 13244 (1992).

[56]J. P. Perdew, D. C. Langreth, and V. Sahni, Phys. Rev. Lett. **38**, 1030 (1977).

[57]D. C. Langreth and J. P. Perdew, Phys. Rev. B **21**, 5469 (1980).

[58]J. P. Perdew, K. Burke, and M. Ernzerhof, Phys. Rev. Lett. **77**, 3865 (1996).

[59]J. P. Perdew, K. Burke, and Y. Wang, Phys. Rev. B **54**, 16533 (1996).

[60]J. Heyd, J. E. Peralta, G. E. Scuseria, and R. L. Martin, J. Chem. Phys. **123**, 174101 (2005).

[61]J. P. Perdew, R. G. Parr, M. Levy, and J. L. Balduz, Jr., Phys. Rev. Lett. **49**, 1691 (1982).

[62]L. J. Sham and M. Schlüter, Phys. Rev. Lett. **51**, 1888 (1983).

[63]J. P. Perdew and M. Levy, Phys. Rev. B **56**, 16021 (1997).

[64]Y. Zhang and W. Yang, J. Chem. Phys. **109**, 2604 (1998).

[65]W. Yang, A. J. Cohen, and P. Mori-Sànchez, J. Chem. Phys. **136**, 204111 (2012).

[66]L. Hedin, Phys. Rev. **139**, A796 (1965).

[67]L. Hedin and S. Lundqvist, in *Solid State Physics*, edited by F. Seitz, D. Turnbull, and H. Ehrenreich, Vol. 23 (Academic Press, New York, 1965).

[68]F. Tran and P. Blaha, Phys. Rev. Lett. **102**, 226401 (2009).

[69] A. D. Becke and E. R. Johnson, J. Chem. Phys. **124**, 221101 (2006).

[70] F. Tran, P. Blaha, and K. Schwarz, J. Phys.: Condens. Matter **19**, 196208 (2007).

[71] A. D. Becke and M. R. Roussel, Phys. Rev. A **39**, 3761 (1989).

[72] A. P. Gaiduk and V. N. Staroverov, J. Chem. Phys. **131**, 044107 (2009).

[73] Y.-S. Kim, M. Marsman, G. Kresse, F. Tran, and P. Blaha, Phys. Rev. B **82**, 205212 (2010).

[74] D. Koller, F. Tran, and P. Blaha, Phys. Rev. B **83**, 195134 (2011).

[75] G. Kresse, M. Marsman, L. E. Hintzsche, and E. Flage-Larsen, Phys. Rev. B **85**, 045205 (2012).

[76] J. C. Slater and K. H. Johnson, Phys. Rev. B **5**, 844 (1972).

[77] J. F. Janak, Phys. Rev. B **18**, 7165 (1978).

[78] S. Sanna, Th. Frauenheim, and U. Gerstmann, Phys. Rev. B **78**, 085201 (2008).

[79] L. G. Ferreira, M. Marques, and L. K. Teles, AIP Adv. **1**, 032119 (2011).

[80] L. G. Ferreira, M. Marques, and L. K. Teles, Phys. Rev. B **78**, 125116 (2008).

[81] M. Ribeiro, Jr., L. R. C. Fonseca, and L. G. Ferreira, Phys. Rev. B **79**, 241312(R) (2009).

[82] M. van Schilfgaarde, T. Kotani, and S. Faleev, Phys. Rev. Lett. **96**, 226402 (2006).

[83] M. Shishkin and G. Kresse, Phys. Rev. B **75**, 235102 (2007).

[84] M. Shishkin, M. Marsman, and G. Kresse, Phys. Rev. Lett. **99**, 246403 (2007).

[85] R. R. Pelá, C. Caetano, M. Marques, L. G. Ferreira, J. Furthmüller, and L. K. Teles, Appl. Phys. Lett. **98**, 151907 (2011).

[86] A. Belabbes, J. Furthmüller, and F. Bechstedt, Phys. Rev. B **84**, 205304 (2011).

[87] A. Belabbes, C. Panse, J. Furthmüller, and F. Bechstedt, Phys. Rev. B **86**, 075208 (2012).

[88] S. Küfner, A. Schleife, B. Höffling, and F. Bechstedt, Phys. Rev. B **86**, 075320 (2012).

[89] M. Ribeiro, Jr., L. R. C. Fonseca, and L. G. Ferreira, Eur. Phys. Lett. **94**, 27001 (2011).

[90] C. Adamo and V. Barone, J. Chem. Phys. **110**, 6158 (1999).

[91] M. Ernzerhof and G. E. Scuseria, J. Chem. Phys. **110**, 5029 (1999).

[92] J. P. Perdew, M. Ernzerhof, and K. Burke, J. Chem. Phys. **105**, 9982 (1996).

[93] J. Heyd, G. E. Scuseria, and M. Ernzerhof, J. Chem. Phys. **118**, 8207 (2003).

[94] J. Heyd and G. E. Scuseria, J. Chem. Phys. **121**, 1187 (2004).

[95] J. Heyd, G. E. Scuseria, and M. Ernzerhof, J. Chem. Phys. **124**, 219906 (2006).

[96] A. V. Krukau, O. A. Vydrov, A. F. Izmaylov, and G. E. Scuseria, J. Chem. Phys. **125**, 224106 (2006).

[97] J. Paier, M. Marsman, K. Hummer, G. Kresse, C. Gerber, and J. G. Ángyán, J. Chem. Phys. **124**, 154709 (2006).

[98] M. Marsman, J. Paier, A. Stroppa, and G. Kresse, J. Phys.: Condens. Matter **20**, 064201 (2008).

[99] T. M. Henderson, J. Paier, and G. E. Scuseria, Phys. Status Solidi B **248**, 767 (2011).

[100] M. Landmann, E. Rauls, and W. G. Schmidt, J. Phys.: Condens. Matter **24**, 195503 (2012).

[101] J. W. Nicklas and J. W. Wilkins, Appl. Phys. Lett. **97**, 091902 (2010).

[102] H. P. Komsa, P. Broqvist, and A. Pasquarello, Phys. Rev. B **81**, 205118 (2010).

[103] W. Chen, C. Tegenkamp, H. Pfnür, and T. Bredow, Phys. Rev. B **82**, 104106 (2010).

[104] H. J. von Bardeleben, J. L. Cantin, U. Gerstmann, A. Scholle, S. Greulich-Weber, E. Rauls, M. Landmann, W. G. Schmidt, A. Gentils, J. Botsoa, and M. F. Barthe, Phys. Rev. Lett. **109**, 206402 (2012).

[105] M. S. Hybertsen and S. G. Louie, Phys. Rev. B **34**, 5390 (1986).

[106] M. Rohlfing and S. G. Louie, Phys. Rev. B **62**, 4927 (2000).

[107] M. Shishkin and G. Kresse, Phys. Rev. B **74**, 035101 (2006).

[108] M. Rohlfing, P. Krüger, and J. Pollmann, Phys. Rev. B **48**, 17791 (1993).

[109] M. Rohlfing, P. Krüger, and J. Pollmann, Phys. Rev. B **56**, R7065 (1997).

[110] F. Caruso, P. Rinke, X. Ren, M. Scheffler, and A. Rubio, Phys. Rev. B **86**, 081102(R) (2012).

[111] T. Kotani, M. van Schilfgaarde, and S. V. Faleev, Phys. Rev. B **76**, 165106 (2007).

[112] P. Romaniello, S. Guyot, and L. Reining, J. Chem. Phys. **131**, 154111 (2009).

[113] K. Momma and F. Izumi, J. Appl. Crystallogr. **44**, 1272 (2011).

[114] K. C. Hass, L. C. Davis, and A. Zunger, Phys. Rev. B **42**, 3757 (1990).

[115] C. Jiang, C. Wolverton, J. Sofo, L.-Q. Chen, and Z.-K. Liu, Phys. Rev. B **69**, 214202 (2004).

[116] C. K. Gan, Y. P. Feng, and D. J. Srolovitz, Phys. Rev. B **73**, 235214 (2006).

[117] D. Shin, R. Arròyave, Z.-K. Liu, and A. Van de Walle, Phys. Rev. B **74**, 024204 (2006).

[118] F. Wang, S.-S. Li, J.-B. Xia, H. X. Jiang, J. Y. Lin, J. Li, and S.-H. Wei, Appl. Phys. Lett. **91**, 061125 (2007).

[119] J. von Pezold, A. Dick, M. Friák, and J. Neugebauer, Phys. Rev. B **81**, 094203 (2010).

[120] A. Van de Walle, M. Asta, and G. Ceder, Calphad: Comput. Coupling of Phase Diagrams and Thermochem. **26**, 539 (2002).

[121] I. Petrov, E. Mojab, R. C. Powell, J. E. Greene, L. Hultman, and J.-E. Sundgren, Appl. Phys. Lett. **60**, 2491 (1992).

[122] M. Mizuta, S. Fujieda, Y. Matsumoto, and T. Kawamura, Jpn. J. Soc. Appl. Phys. **25**, L945 (1986).

[123] Y. Koide, H. Itoh, N. Sawaki, I. Akasaki, and M. Hashimoto, J. Electrochem. Soc. **133**, 1956 (1986).

[124] L. K. Teles, J. Furthmüller, L. M. R. Scolfaro, J. R. Leite, and F. Bechstedt, Phys. Rev. B **62**, 2475 (2000).

[125] G. Kresse and J. Furthmüller, Comput. Mater. Sci. **6**, 15 (1996).

[126] P. E. Blöchl, Phys. Rev. B **50**, 17953 (1994).

[127] G. Kresse and D. Joubert, Phys. Rev. B **59**, 1758 (1999).

[128] L. C. de Carvalho, A. Schleife, F. Fuchs, and F. Bechstedt, Appl. Phys. Lett. **97**, 232101 (2010).

[129] L. C. de Carvalho, A. Schleife, and F. Bechstedt, Phys. Rev. B **84**, 195105 (2011).

[130] M. Feneberg, M. F. Romero, B. Neuschl, K. Thonke, M. Röppischer, C. Cobet, N. Esser, M. Bickermann, and R. Goldhahn, Appl. Phys. Lett. **102**, 052112 (2013).

[131] S. A. Ding, G. Neuhold, J. H. Weaver, P. Häberle, and K. Horn, J. Vac. Sci. Technol. A **14**, 819 (1996).